




Article

The Effect of Noble Metal (M: Ir, Pt, Pd) on M/Ce₂O₃-γ-Al₂O₃ Catalysts for Hydrogen Production via the Steam Reforming of Glycerol

Nikolaos D. Charisiou ^{1,*}, Georgios I. Siakavelas ¹, Kyriakos N. Papageridis ¹, Davide Motta ², Nikolaos Dimitratos ³ , Victor Sebastian ^{4,5} , Kyriaki Polychronopoulou ^{6,7} and Maria A. Goula ^{1,*} 

¹ Laboratory of Alternative Fuels and Environmental Catalysis (LAFEC), Department of Chemical Engineering, University of Western Macedonia, 50100 Kozan, Greece; giorgosiakavelas@gmail.com (G.I.S.); kpapageridis@gmail.com (K.N.P.)

² Cardiff Catalysis Institute, School of Chemistry, Cardiff University, Cardiff CF10 3AT, UK; MottaD@cardiff.ac.uk

³ Dipartimento di Chimica Industriale “Toso Montanari”, Università degli Studi di Bologna, 40136 Bologna, Italy; Nikolaos.dimitratos@unibo.it

⁴ Chemical and Environmental Engineering Department, Instituto de Nanociencia de Aragón (INA) and Instituto de Ciencia de Materiales de Aragón (ICMA), Universidad de Zaragoza-CSIC, 50018 Zaragoza, Spain; victorse@unizar.es

⁵ Networking Research Center on Bioengineering, Biomaterials and Nanomedicine, CIBERBBN, 28029 Madrid, Spain

⁶ Department of Mechanical Engineering, Khalifa University of Science and Technology, Abu Dhabi 127788, UAE; kyriaki.polychrono@ku.ac.ae

⁷ Center for Catalysis and Separations, Khalifa University of Science and Technology, Abu Dhabi 127788, UAE

* Correspondence: ncharis@teiwm.gr (N.D.C.); mgoula@uowm.gr (M.A.G.); Tel.: +30-24610-68296 (N.D.C. & M.A.G.)

Received: 19 June 2020; Accepted: 14 July 2020; Published: 15 July 2020



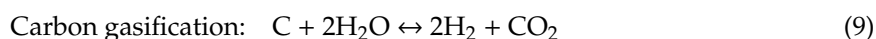
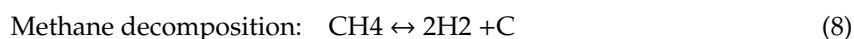
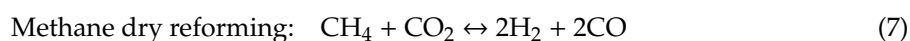
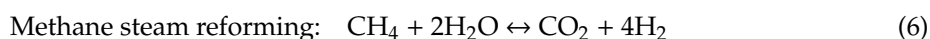
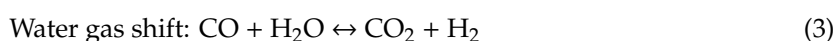
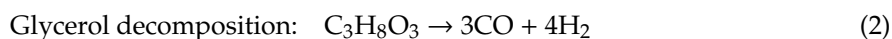
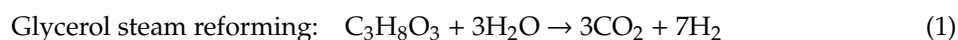
Abstract: A promising route for the energetic valorisation of the main by-product of the biodiesel industry is the steam reforming of glycerol, as it can theoretically produce seven moles of H₂ for every mole of C₃H₈O₃. In the work presented herein, CeO₂-Al₂O₃ was used as supporting material for Ir, Pd and Pt catalysts, which were prepared using the incipient wetness impregnation technique and characterized by employing N₂ adsorption-desorption, X-Ray Diffraction (XRD), Temperature Programmed Reduction (TPR), Temperature Programmed Desorption (TPD), X-ray Photoelectron Spectroscopy (XPS) and Transmission Electron Microscopy (TEM). The catalytic experiments aimed at identifying the effect of temperature on the total conversion of glycerol, on the conversion of glycerol to gaseous products, the selectivity towards the gaseous products (H₂, CO₂, CO, CH₄) and the determination of the H₂/CO and CO/CO₂ molar ratios. The main liquid effluents produced during the reaction were quantified. The results revealed that the Pt/CeAl catalyst was more selective towards H₂, which can be related to its increased number of Brønsted acid sites, which improved the hydrogenolysis and dehydrogenation-dehydration of condensable intermediates. The time-on-stream experiments, undertaken at low Water Glycerol Feed Ratios (WGFR), showed gradual deactivation for all catalysts. This is likely due to the dehydration reaction, which leads to the formation of unsaturated hydrocarbon species and eventually to carbon deposition. The weak metal-support interaction shown for the Ir/CeAl catalyst also led to pronounced sintering of the metallic particles.

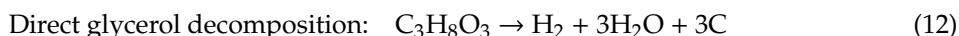
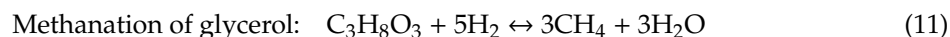
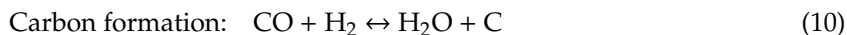
Keywords: glycerol steam reforming; Pt catalysts; Ir catalysts; Pd catalysts; ceria-alumina support

1. Introduction

Anthropogenic dominance over the planet is so profound that the term ‘anthropocene’ has been proposed as a more apt description of the current geological epoch. Although the consequences of the impact of anthropos are catastrophic for the global sum of ecosystems, i.e., atmosphere, hydrosphere, lithosphere and biosphere, the issue of global climate change—caused by our insatiable appetite for petro-based energy—is perhaps causing the greatest agony over humanity’s future well being. Arguably, despite making significant progress in substituting fossil energy with Renewable Energy Systems (RES) for electricity production, in the transport sector petro-energy retains a protagonists’ role, with current efforts in finding an alternative relying on the development of starch- and sugar-based ethanol, deoxygenation for the production of bio-hydrogenated diesel, and fatty acid methyl ester (FAME) biodiesel [1–4]. Although it’s not a hyperbole to describe the advancement of the biodiesel industry as phenomenal—the sector achieved growth rates of almost 25% per annum between 2005 and 2015, leading to a seven-fold expansion during a single decade—biofuels account for less than 7% of fuels used in the transport sector [5,6]. Moreover, the production of crude glycerol, the main by-product of the transesterification reaction, has also expanded synchronously, hanging like an anathema over the sustainable credentials of the industry [7,8].

As glycerol ($C_3H_8O_3$) is a polyol with three hydroxyl groups, it may be possible to utilize it in a plethora of industrial platforms (Bagheri et al. [9] has provided an excellent review on the different technological pathways that are currently being developed) however, the pressing need for further ‘greening’ of the energy sector, means that its conversion to hydrogen via thermochemical processes (i.e., via pyrolysis or different reforming reactions) is perhaps the most attractive option [10–13]. As is widely accepted, hydrogen is an efficient energy carrier that can provide clean power in stationary, portable and transport applications [14,15]. Thus, the steam reforming of glycerol (GSR) has been enthusiastically researched over the past few years because, as it is clear from the overall reaction (Equation (1)), one mole of $C_3H_8O_3$ can, in theory, produce seven moles of H_2 . It is noted that Equation (1) is endothermic ($\Delta H^0 = 123 \text{ kJ mol}^{-1}$) and combines the decomposition of $C_3H_8O_3$ (Equation (2)), which is also endothermic ($\Delta H^0 = 245 \text{ kJ mol}^{-1}$) and the water–gas shift (WGS, Equation (3)), an exothermic reaction ($\Delta H^0 = -41 \text{ kJ mol}^{-1}$). $C_3H_8O_3$ decomposition occurs at temperatures exceeding 300°C and can involve different parallel and/or consecutive steps, which not only include the cleavage of the C–C and C–O bonds, but also dehydration, dehydrogenation, hydrogenation, isomerisation and polymerisation reactions [16,17]. Additionally, depending on the operating conditions and/or the catalytic system under consideration, a number of other reactions may also parallelly occur, such as, CO methanation (Equation (4)), CO disproportionation (Equation (5)), methane reforming (Equations (6) and (7)) carbon formation (Equations (8)–(10)), methanation of glycerol (Equation (11)) and direct glycerol decomposition (Equation (12)) [18–20].





Apart from the possibility of obtaining high H_2 yields, the GSR has two additional advantages; it is a mature industrial technology (the steam reforming of methane and naphtha generate 48% and 30%, respectively, of the commercially produced H_2 , thus switching feedstocks should not pose insurmountable challenges for the industry) and as thermodynamics predict, its best utilised at atmospheric pressure [21,22]. According to the latter studies (i.e., thermodynamics) the yield to hydrogen maximises at relatively high temperatures ($<630^\circ\text{C}$) and high water to glycerol feed ratios (WGFR, $<9:1$, molar); at such conditions the maximum attainable H_2 yield is 6.2 (mole of H_2 per mole of $\text{C}_3\text{H}_8\text{O}_3$) [20,23,24].

The catalyst system chosen for use in the GSR should have the capacity to promote the cleavage of C–C, O–H, and C–H bonds in the $\text{C}_3\text{H}_8\text{O}_3$ molecule and inhibit that of the C–O bonds (as this would lead to the production of alkenes and thus, the formation of carbon). The catalyst used should also promote the WGS reaction, as this would allow the absorbed surface CO to be removed as CO_2 [25,26]. As a result, numerous efforts at identifying the most appropriate catalytic systems have been carried out, with the majority of reports focusing on the development of Ni catalysts based on a variety of different metal oxides (e.g., Al_2O_3 , SiO_2 , La_2O_3 , CeO_2 , ZrO_2) and/or the use of transition metals (e.g., ZrO_2 , Co, Cu), lanthanide metals (e.g., La, Ce) or alkaline earth metals (e.g., Ca, MgO, Ba) as modifiers in the supports. The exegesis for the focus on Ni lies with the fact that it is a widely available metal (thus, inexpensive) and also that it shows very high intrinsic activity when well dispersed on to the support [27–36]. Moreover, Ni promotes the cleavage of C–C, O–H, and C–H bonds (in the order of O–H, $-\text{CH}_2-$, C–C, $-\text{CH}_3$) [22], as well as dehydrogenation and hydrogenation [27,28]. However, despite the reporting of some very promising results [30–35], at high temperatures, Ni-based catalysts are also susceptible to carbon deposition and metal particle sintering, which unavoidably leads to their eventual deactivation [36,37].

Due to the high cost of noble metal catalysts, their use is limited, despite the fact that such systems usually show high catalytic activity and low carbon formation during steam reforming reactions. Most of the works reported in the literature for the GSR have focused on ruthenium [38–43], as Ru is the least expensive among all noble metals, and platinum [44–51], but one may also find a few works that have examined the performance of Rh [52–55], Ir [56] or Pd [57] catalysts. However, there are only a handful of works that perform a comparative assessment of the performance of different noble metal catalysts [58,59]. One of the earliest such works was reported by Adhikari et al. [58] who compared the performance of Rh, Pt, Pd, Ir, Ru and Ni catalysts supported on (i) commercial alumina ceramic foam monoliths and, (ii) the same alumina monoliths modified with CeO_2 . However, the catalysts were not activated prior to reaction, resulting in poor glycerol conversion and H_2 selectivity. Senseni et al. [59] examined the performance of Rh, Ru, Pt, Ir (1 wt.%) catalysts supported on Al_2O_3 modified with MgO, between 300 and 600°C , and showed that glycerol conversion followed the order $\text{Rh} > \text{Pt} > \text{Ru} > \text{Ir}$, while H_2 selectivity was $\text{Rh} > \text{Ir} > \text{Ru} > \text{Pt}$. Time-on-stream tests were carried out only on the Rh catalysts, demonstrating that the catalyst was stable over time.

In addition to the choice of active metal, the support also affects the activity and stability characteristics of a catalytic system. In general, dispersion is aided when the support has a high surface area and can provide strong metal support interactions (SMSI). On the other hand, a high surface area means that the pore size distribution will likely be small (inhibiting intra-particle diffusion of reactants and products), while too strong interaction will negatively affect the reducibility of the active metal. The acidity/basicity characteristics of the supporting material are also crucial parameters, as methane decomposition (Equation (8)), which leads to carbon formation, is favoured over the acid sites of the support, while CO_2 activation, which removes the deposited coke, occurs over the basic sites [60–62].

Alumina, at first approximation, is an attractive support for GSR catalysts as it possesses a relatively high surface area, and can also provide mechanical and chemical resistance during the reaction [63,64]. Moreover, due to its acid character, alumina also promotes dehydration, polymerization and isomerisation, which take place during the GSR. However, alumina also induces carbon deposition and sintering; the former is caused by the promotion of cracking reactions, while the latter can occur through the transition of Al_2O_3 to a crystalline phase during high temperature reactions [30,31,39,60]. Thus, the acid character of Al_2O_3 must be tuned in order to help promote the desired reactions, while at the same time avoid carbon deposition and sintering.

Cerium oxide, although thermally unstable [65], is known to possess high oxygen storage capacity (OSC) and redox properties ($\text{Ce}^{4+}/\text{Ce}^{3+}$) that help to improve the dispersion of the active sites and decrease carbon deposition on the catalyst surface by promoting carbon oxidation reactions. Moreover, CeO_2 can help to achieve strong interaction with the supported metal (improving the stability of the active phase against sintering), and also increase basicity, which leads to the adsorption and activation of CO_2 on the support sites [66–70].

Profeti et al. [62] studied the catalytic activity of Ni catalysts supported on $\text{CeO}_2\text{--Al}_2\text{O}_3$ that was modified with noble metals (Pt, Ir, Pd and Ru) during the GSR and reported that the presence of cerium oxide helped prevent the formation of inactive nickel aluminate, thus helping to enhance performance; their results showed that the highest glycerol conversion was achieved by the NiPd/CeAl and NiPt/CeAl samples. Demsash et al. [71] prepared Ni/CeAl catalysts and examined the effect of Ni (5, 10 and 15 wt.%) and CeO_2 (5 and 10 wt.%) loadings and found that the best results were achieved by the 10Ni/ Al_2O_3 /5 CeO_2 ; they thus argued that an optimal CeO_2 (and Ni) loading exists. Iriondo et al. [72] studied the GSR using Ni catalysts supported on bare CeO_2 and Al_2O_3 , and alumina modified with ceria and showed that the incorporation of low ceria loadings, i.e., 5 and 10 wt.%, resulted in enhanced catalytic activity, as CeO_2 helped to stabilize the active phase through strong Ni– CeO_2 interactions; at higher CeO_2 loadings performance declined in agreement with the work of Profeti et al. [62]. Kamonsuangkasem et al. [73] prepared $\text{CeO}_2\text{--Al}_2\text{O}_3$ mixed oxides and used them as supports for Ni-based catalysts (tested in the GSR). The authors reported that by using a sol–gel preparation method, they were able to incorporate the Ce species into the Al_2O_3 structure, forming a CeAlO_3 perovskite, which suppressed the interaction between the active phase and alumina and thus, led to the formation of an enhanced number of active sites. Moreover, the incorporation of CeO_2 into the support helped increase the number of Brønsted acid sites, which improved the hydrogenolysis and dehydrogenation–dehydration of condensable intermediates, leading to improved H_2 production. Chen et al. [74], has also reported that the formation of CeAlO_3 enhanced considerably the catalyst's resistance to carbon deposition during the reforming of CH_4/CO_2 .

Prompted by the above, we have proceeded in preparing a $\text{CeO}_2\text{--Al}_2\text{O}_3$ support (10 wt.%), which we then used to synthesize low loading Pt, Pd and Ir catalysts (0.5 wt.%); the support and the catalysts were prepared via the incipient wetness impregnation technique. The materials were then examined in terms of catalytic activity and time-on-stream stability for the glycerol steam reforming reaction. The characterization techniques that were used to identify the catalysts' surface and bulk properties that affect the reaction's products included N_2 adsorption–desorption, X-Ray Diffraction (XRD), Temperature Programmed Reduction (TPR), Temperature Programmed Desorption (TPD), X-ray Photoelectron Spectroscopy (XPS) and Transmission Electron Microscopy (TEM). The catalytic experiments aimed at identifying the effect of temperature on the total conversion of glycerol, on the conversion of glycerol to gaseous products, the selectivity towards the gaseous products (H_2 , CO_2 , CO , CH_4) and the determination of the H_2/CO and CO/CO_2 molar ratios. Moreover, we identified and quantified the liquid effluents produced during the reaction. Time-on-stream experiments were conducted for 8 h at harsh reaction conditions in order to induce catalyst deactivation and the spent catalysts were examined using TEM analysis.

2. Results and Discussion

2.1. Characterizations Results

Table 1 shows the specific surface area ($\text{m}^2 \text{g}^{-1}$), pore volume ($\text{cm}^3 \text{g}^{-1}$) and average pore width (nm) of the calcined catalytic samples used herein. As can be seen, the Ir/CeAl, Pd/CeAl and Pt/CeAl catalysts present comparable values for specific surface area ($163\text{--}179 \text{ m}^2 \text{g}^{-1}$), pore volume ($0.27\text{--}0.30 \text{ cm}^3 \text{g}^{-1}$) and average pore width ($14.0\text{--}17.4 \text{ nm}$). Moreover, as can be seen in Figure 1, all catalysts present isotherms of Type IV(a) and hysteresis loops of $\text{H}_2(\text{b})$ type, displaying minimal adsorption at the low pressure range ($P/P_0 < 0.06$) and substantial adsorption at higher pressures ($0.6 < P/P_0 < 1.0$). This is indicative of mesoporous materials with some macroporous structures [30]. This conclusion is further verified by the BJH adsorption data and the corresponding pore size distribution curves (inset of Figure 1), showing that the majority of the population of pores is in the meso-range.

Table 1. Morphological and textural properties for the prepared catalysts.

Catalyst	SSA ($\text{m}^2 \text{g}^{-1}$)	Pore Volume ($\text{cm}^3 \text{g}^{-1}$)	Av. Pore Width (nm)
Ir/CeAl	179	0.30	17.4
Pd/CeAl	167	0.27	14.0
Pt/CeAl	163	0.28	15.5

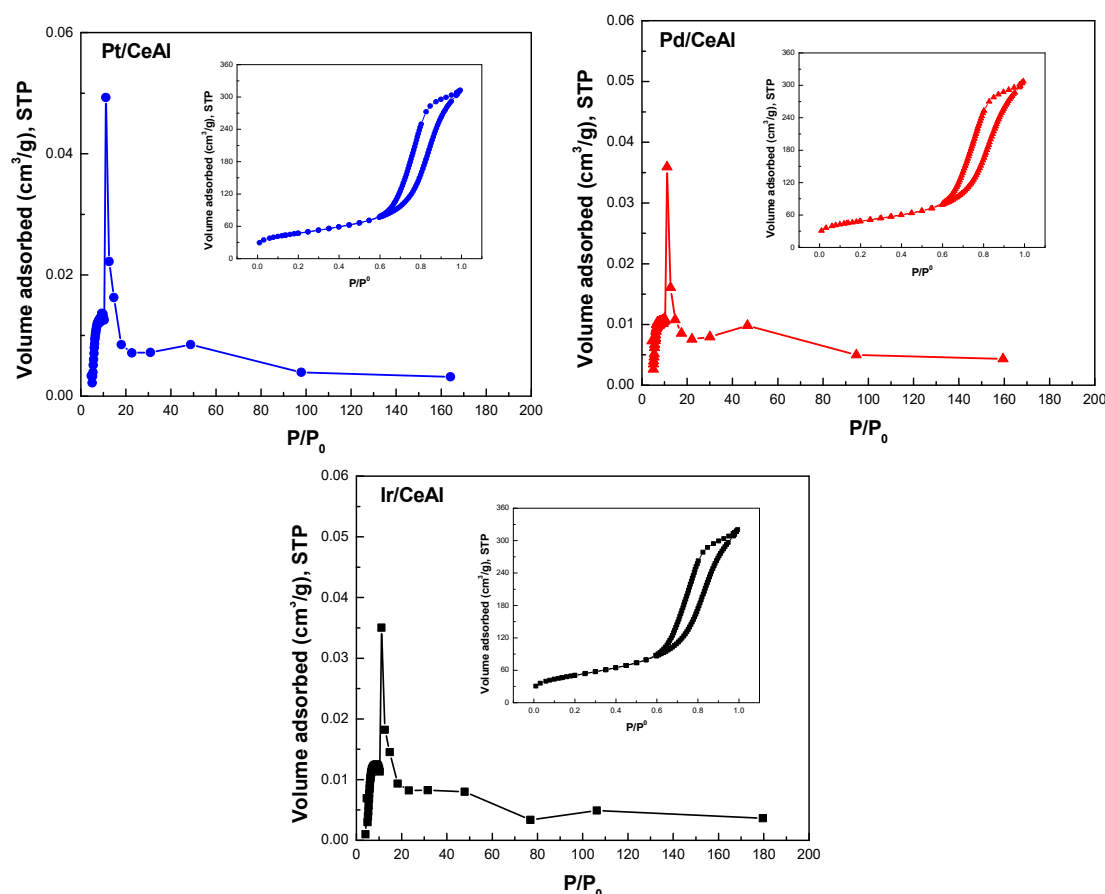


Figure 1. Pore size distribution and N_2 adsorption–desorption isotherms (inset) of the calcined Pt/CeAl, Pd/CeAl and Ir/CeAl catalysts.

The XRD patterns of the calcined Pt/CeAl, Pd/CeAl and Ir/CeAl catalytic samples are depicted in Figure 2. As can be seen, all the catalysts showed substantial diffraction peaks at $2\theta = 28.5^\circ$, 33.0° , 47.6° , 56.4° and 59.0° which correspond to the (111), (200), (220) and (311) planes of the cubic fluorite

structure of cerium oxide (JCPDS Card No.: 96-900-9009) and at $2\theta = 34.0^\circ$ (220), 37.7° (311), 45.0° (400) and 67.0° (440), corresponding to the crystal structure of γ -Al₂O₃ (JCPDS Card No.: 96-900-7636) [70]. From the XRD pattern of the Ir/CeAl catalyst, characteristic diffraction peaks of highly crystalline particles of IrO₂ at $2\theta = 28.0^\circ$ and 54.0° can also be clearly observed, which correspond to the (110) and (211) planes [75]. On the other hand, no diffraction peaks related to PtO₂ (expected at $2\theta = 33.3^\circ$ and 55.9°) or PdO (expected at $2\theta = 34.7^\circ$ and 54.8°) are observed on the diffractograms of Pt/CeAl and Pd/CeAl. However, as will be described below, these species were detected during the TPR and XPS experiments of the calcined and reduced catalysts [76]. The absence of the characteristic diffraction peaks of the PtO₂ and PdO may be caused by a number of reasons, i.e., the low concentration of the metal oxides in the supporting material, the possible formation of amorphous structures or interfacial solid solutions, the increased dispersion of PtO₂ and/or PdO on the catalyst surface or finally, the formation of microscopic crystalline sizes, which escape from the XRD detection [77].

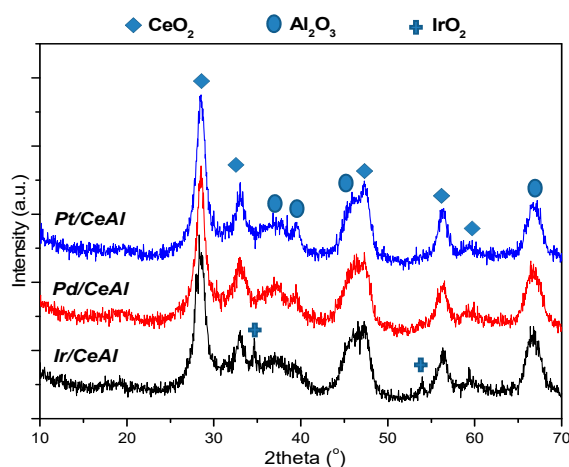


Figure 2. XRD patterns of the calcined Pt/CeAl, Pd/CeAl and Ir/CeAl catalysts.

The H₂-TPR experiments (Figure 3) were carried out with the purpose of investigating the strength of the interaction (electronic or geometrical) between the CeO₂–Al₂O₃ support and the active metal sites (Ir, Pt and Pd). The interactions are anticipated to affect the reducibility of the metal oxides, and as a result, influence their catalytic performance in terms of glycerol conversion, H₂ selectivity and yield. From Figure 3 shown herein, reduction peaks at low (100–300 °C), medium (300–600 °C) and high temperatures (600–800 °C) can be observed. According to the literature [28], the created weak metal–support interactions are related with the genesis of reduction peaks at low temperature, while peaks at medium and high temperature are attributed to the existence of medium and strong metal–support interaction, respectively. Furthermore, the reduction of cerium oxide occurs at ≈ 500 and 830°C for the surface and the bulk oxygen species, respectively [78]. For the Ir and Pd catalysts, reduction peaks were observed at 150°C and in the temperature range of 200 – 300°C , indicating either smaller Ir and/or Pd particles size (better dispersion of active sites) or the existence of weaker interaction between the active sites with the supporting material, leading to an easier reduction [25]. On the other hand, the Pt-based catalyst presented larger peaks at higher reduction temperature, probably due to the reduction of various PtO_x-oxides interacting with the support under different metal–support interactions or to the easier reduction of CeO₂. Duarte et al. [79] reported that the first two peaks can be attributed to the reduction in highly dispersed Pt oxide species with different interaction with the supporting material including some isolated platinum ions, while the third peak centred at higher temperature can be assigned to the reduction in bulk-like or clustered platinum oxide species. Furthermore, Damyanova et al. [80] showed that the reduction peaks at 200 – 320°C may be attributed to Pt particles with a non-uniform size distribution and to the formation of non-stoichiometric cerium

oxide; they also reported that the presence of platinum particles on the catalyst surface causes the easier reduction in cerium oxide at lower temperature.

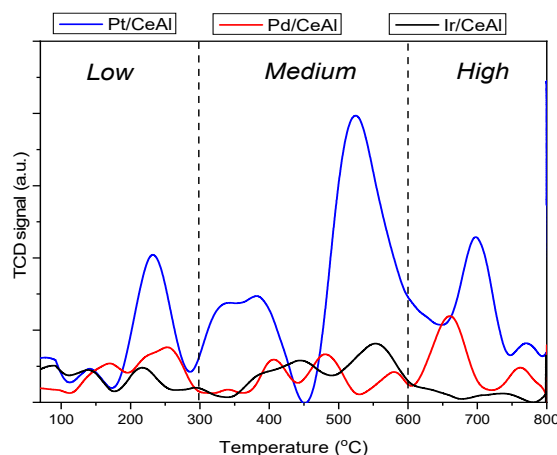


Figure 3. H₂-TPR profiles of the calcined Ir/CeAl, Pd/CeAl and Pt/CeAl catalysts.

Temperature programmed desorption of CO₂ (Figure 4), was performed after pre-treatment in oxygen atmosphere and at room temperature (25 °C) and aimed at investigating the number and strength of basic sites on the catalytic samples tested herein. According to published studies [81], the basic sites can be categorized based on their strength, to weak (50–200 °C), intermediate (200–400 °C), strong (400–650 °C) and very strong (>650 °C) regions. As can be seen in Figure 4a, the CO₂ desorption profile of the Pt/CeAl catalyst showed that the majority of basic sites are located mainly at higher desorption temperature due to the presence of strong and very strong basic sites on the catalyst surface. However, some thermal decomposition of carbonates cannot be excluded for the peak centred at temperature higher than 650 °C [82]. On the other hand, the Ir/CeAl catalysts presented the highest intensity of desorbed CO₂ at low temperature (~200°C) due to the creation of weaker bonds between its surface and CO₂. As for the Pd-based catalyst, it seems to present a uniform distribution between weak, intermediate and strong basic sites. According to the literature [30,83], in steam reforming reactions, increased basicity on the catalyst surface has the ability to enhance the transformation of oxygenated hydrocarbon compounds (OHCs) into H₂ and CO₂, increasing the overall catalytic activity in terms of desirable gaseous products.

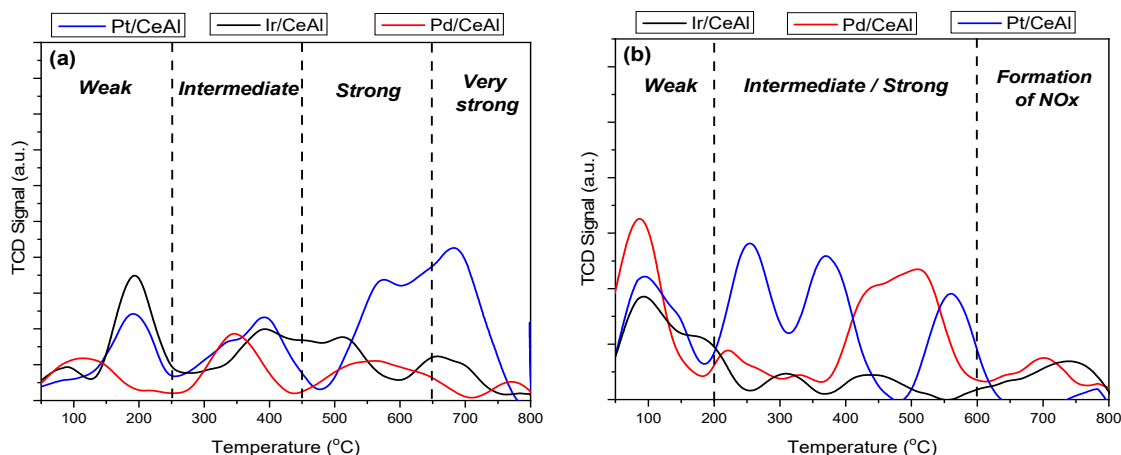


Figure 4. (a) CO₂-TPD, and (b) NH₃-TPD profiles of the Ir/CeAl, Pd/CeAl and Pt/CeAl calcined catalysts.

Temperature-programmed desorption of NH₃ was performed to estimate the concentration and the character of the acid sites, as well as the total acidity of the catalytic materials. As can be seen

in Figure 4b, all the catalysts present a very well-defined acid sites distribution in the temperature range between 50 and 800 °C. Analytically, the TPD-NH₃ profiles show at least three NH₃ desorption areas; the first, located at lower temperatures (<200 °C), can be assigned to weak acid sites, the second, located at medium desorption temperatures (200–600 °C), can be separated to intermediate and strong acid sites, while the third region, at temperature above 600 °C, may be assigned to the possible reaction of NH₃ towards NO_x formation [84]. Though, it has to be mentioned here that the NO_x formation can only be speculated as the experiment was monitored through TCD detector and not through e.g., mass spectrometry. Despite this, it is still a valid speculation if one considers the adsorption and successive dehydrogenation of NH₃ over these catalysts. At the same time, ceria, which is a reducible oxide, is anticipated to provide labile oxygen species and this phenomenon is intensified as the temperature is increased (ca. above 600 °C). According to published studies [28,85], NH₃ desorbed at lower temperature can be linked to physisorbed ammonia on weak acid sites, while NH₃ desorbed at intermediate temperature (200–600 °C) can be associated with the presence of Brønsted acid sites and the presence of stronger acid sites. From the TPD-NH₃ profiles of the catalytic materials tested herein, the Pt/CeAl presents the larger population of Brønsted acid sites and physisorbed ammonia on weak acid sites, followed by the Pd/CeAl and Ir/CeAl catalysts. This is expected to have important implications for the GSR, as increased number of Brønsted acid sites help improve the hydrogenolysis and dehydrogenation–dehydration of condensable intermediates, leading to improved H₂ production [73]. Moreover, literature reports suggest that the catalysts' surface acidity affects the metal particle size. Specifically, Jeon et al. [86] investigated the correlation between the weak Brønsted acid sites and metal particle size and concluded that the increase in the number of the former for the SiO₂–Al₂O₃ was responsible for the formation of smaller Pt crystallite size, leading to higher methane selectivity. Given that alumina thermal treatment leads to de-hydroxylation in the 250–550 °C range (depending on the alumina phases present) [87], most likely no de-hydroxylation would be expected above 600 °C. This could be investigated using sophisticated analysis, such as solid state NMR, FTIR or theoretical calculations [88] as de-hydroxylation leads to the formation of 3-(strong), 4-(medium) and 5-(weak) coordinate Al Lewis acid sites, the coordination environment of which can be studied with the above-mentioned techniques.

XPS analysis (Figure 5 and Table 2) was employed in order to derive information over the surface elemental atomic concentration and the states of the impregnated elements of the reduced catalysts. For the Pt/CeAl (Figure 5c) catalyst, peaks at 72.5–73.1 eV can be attributed to Pt²⁺ 4f_{7/2}, while peaks located at 70.4–71.1 eV can be assigned to Pt⁰ 4f_{7/2} [89]. However, as the binding energies of Al 2p and Pt 4f overlap, the high amount of Al precludes any clear quantification of Pt species. For the Pd/CeAl catalyst (Figure 5b), the two peaks observed can be attributed to Pd 3d_{5/2} (at 334.9 eV) and Pd 3d_{3/2} (at 340.4 eV), which correspond to Pd⁰ [90]. The binding energy of Pd 3d_{5/2} was at 334.9 eV, indicating the presence of Pd in metallic state, and with an atomic surface concentration equal to 0.11%. For the Ir/CeAl catalyst (Figure 5a) two peaks can be observed, proving the presence of Ir 4f_{7/2} (at 60.6 eV) and Ir 4f_{5/2} (at 63.7 eV), which corresponds to Ir in the metallic state and with an atomic surface concentration equal to 0.08% [91].

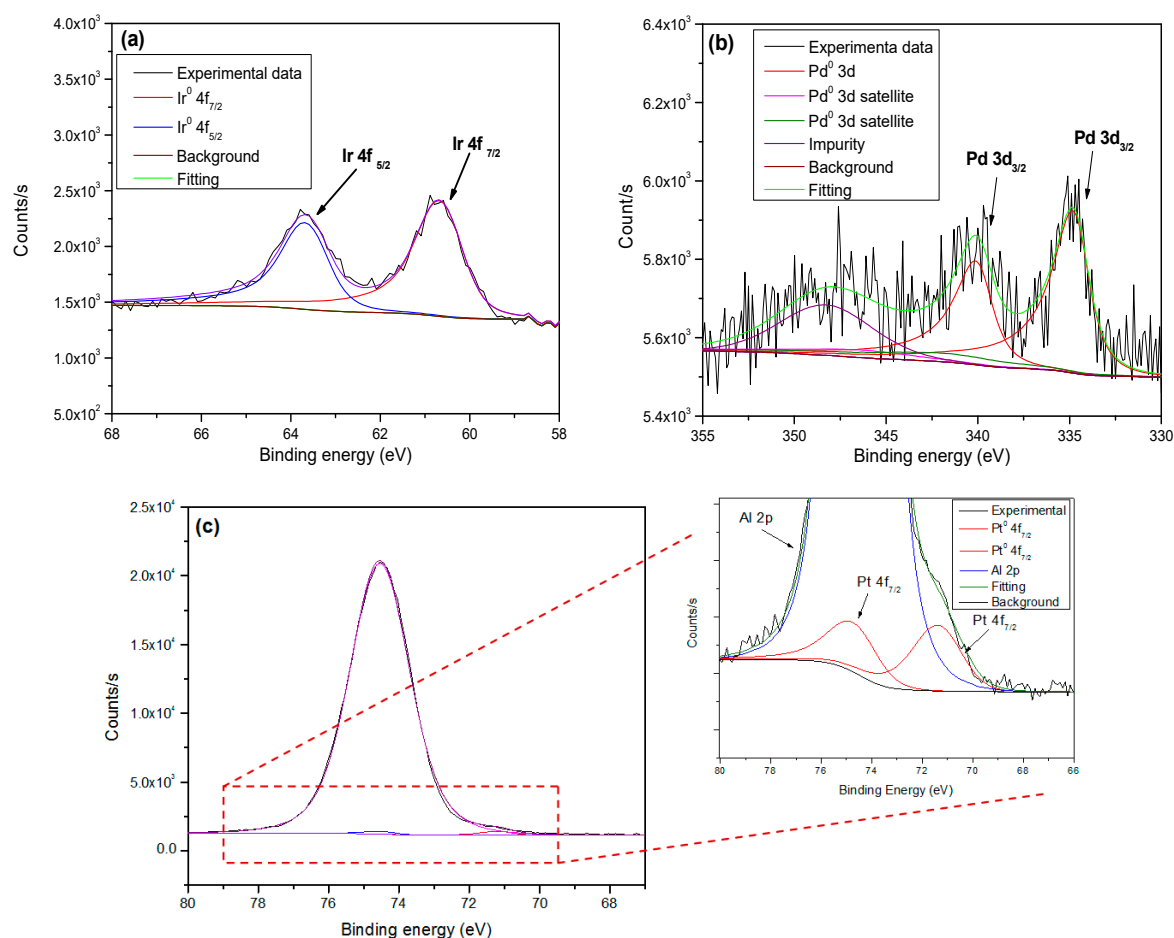


Figure 5. (a) Ir 4f spectra of the Ir/CeAl, (b) Pd 3d spectra of Pd/CeAl and (c) Al 2p / Pt 4f of the Pt/CeAl reduced catalysts.

Table 2. XPS data of the reduced catalysts.

Sample	Pd ⁰ , Ir ⁰ , Pt ⁰ Position (eV)	Pd ^{II} , Ir ^{IV} , Pt ^{II} Position (eV)	Pd ⁰ /Pd ^{II} , Ir ⁰ /Ir ^{IV} , Pt ⁰ /Pt ^{II}	Metal at. % on Surface
Pd/CeAl	334.9	—	All Pd ⁰	0.11
Ir/CeAl	60.6	—	All Ir ⁰	0.08
Pt/CeAl	71.1	*	*	0.02

* As Al 2p and Pt 4f have the same binding energy, high amount of Al do not permit a clear quantification of Pt⁺ species.

Figure 6 shows the high-angle annular dark-field–scanning transmission electron microscope HAADF–STEM images, particle size distribution histograms and EDS spectra obtained for the reduced Ir/CeAl (Figure 6a), Pd/CeAl (Figure 6b) and Pt/CeAl (Figure 6c) catalysts. HAADF–STEM images have Z-contrast, where heavy atoms have high brightness. The elemental analysis revealed the presence of Al and Ce on all catalysts and Ir, Pd and Pt on the corresponding samples, as anticipated. C and Cu were also detected on all samples due to the TEM grid-support used for the analysis. The mean particle size followed the order Ir/CeAl > Pd/CeAl (3.7 ± 2.0 nm) > Pt/CeAl (1.1 ± 0.2 nm); the latter catalyst also shows a very narrow Pt size distribution. Regarding the Ir/CeAl catalyst, the particle size histogram (Figure 6a) depicts the presence of two main populations (multimodal distribution): (i) (1.6 ± 0.4 nm), and (ii) (11.8 ± 6.6 nm).

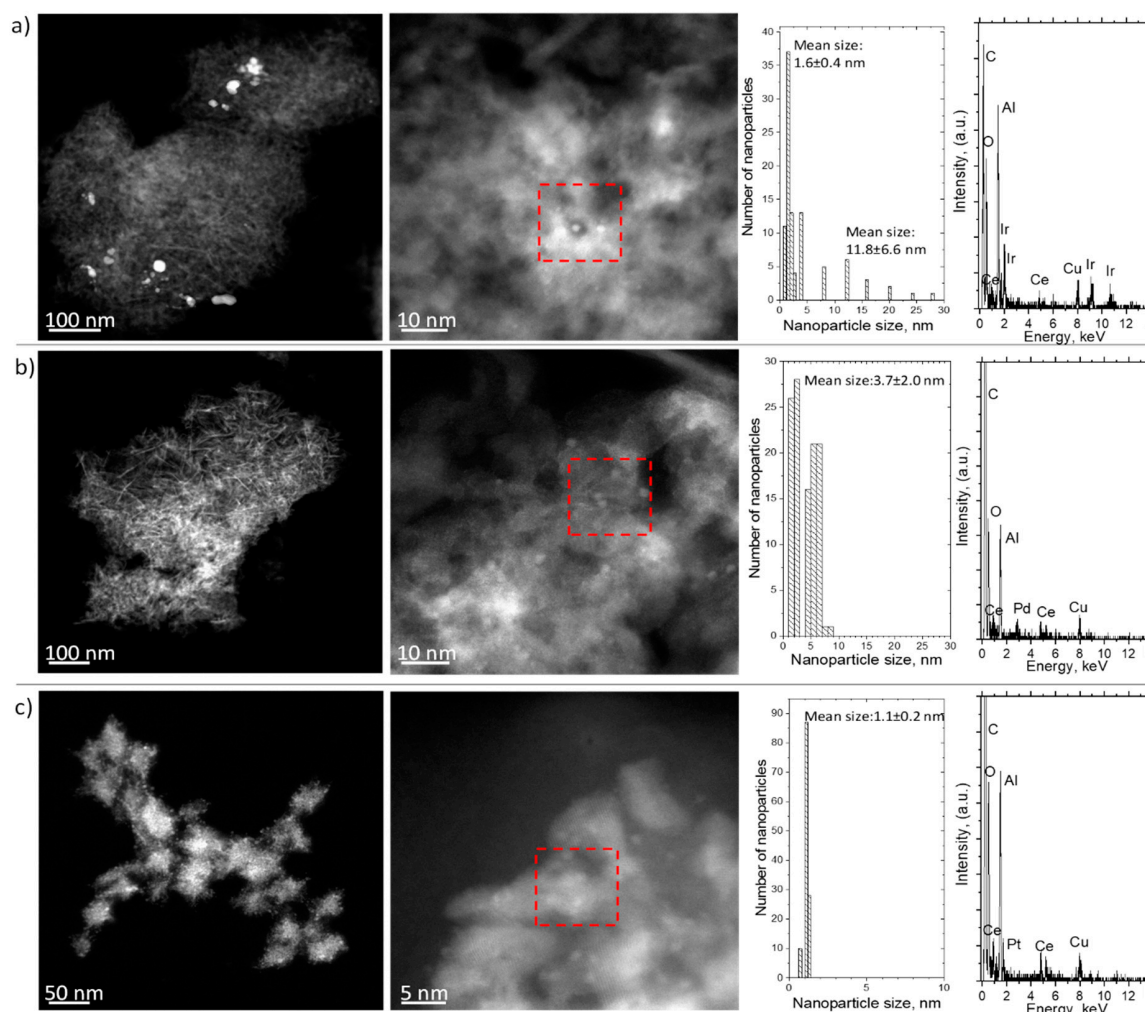


Figure 6. HAADF-STEM images, particle size distribution and EDS spectrum of red-dashed area marked of the reduced: (a) Ir/CeAl, (b) Pd/CeAl, and (c) Pt/CeAl catalysts.

2.2. Catalytic Activity and Selectivity

The activity and selectivity of the catalytic samples was examined at atmospheric pressure between 400 and 750 °C using a WGFR equal to 20:1 (molar) in a continuous flow fixed-bed reactor. Catalytic activation was carried out in situ (prior to catalytic testing) under a flow of high purity H_2 at 800 °C for 1 h (more details of the experimental procedure followed are given in Section 3.3 below). Figure 7 shows, for all catalysts tested herein, the influence of reaction temperature on the total conversion of $C_3H_8O_3$ ($X_{C_3H_8O_3}$, Figure 7a), on the conversion of $C_3H_8O_3$ into gaseous products ($X_{C_3H_8O_3, \text{ gaseous}}$, Figure 7a), on the H_2 selectivity and yield (S_{H_2} and Y_{H_2} , respectively, Figure 7b), the selectivity to CO_2 and CO (S_{CO_2} and S_{CO} , Figure 7c), the selectivity to CH_4 (S_{CH_4} , Figure 7d), and on the H_2/CO (Figure 7e) and CO/CO_2 molar ratio (Figure 7f); H_2 , CO_2 , CO and CH_4 were the only gaseous products identified in any significant concentrations (traces of C_2H_4 were also identified, but not quantified), in agreement with literature reports [37,46,47,49]. It is also noted that as $C_3H_8O_3$ is thermally unstable, the extent of pyrolysis phenomena has a significant role in the GSR, for example Buffoni et al. [45] reported that the thermal decomposition of glycerol could reach 30% molar at 650 °C (for a feed containing 30 wt.% glycerol) and Pompeo et al. [49] 5% molar at 450 °C (for a feed containing 10 wt.% glycerol). Moreover, it is possible that the intermediates formed during the $C_3H_8O_3$ cracking are reformed on the catalysts' surface [31,49].

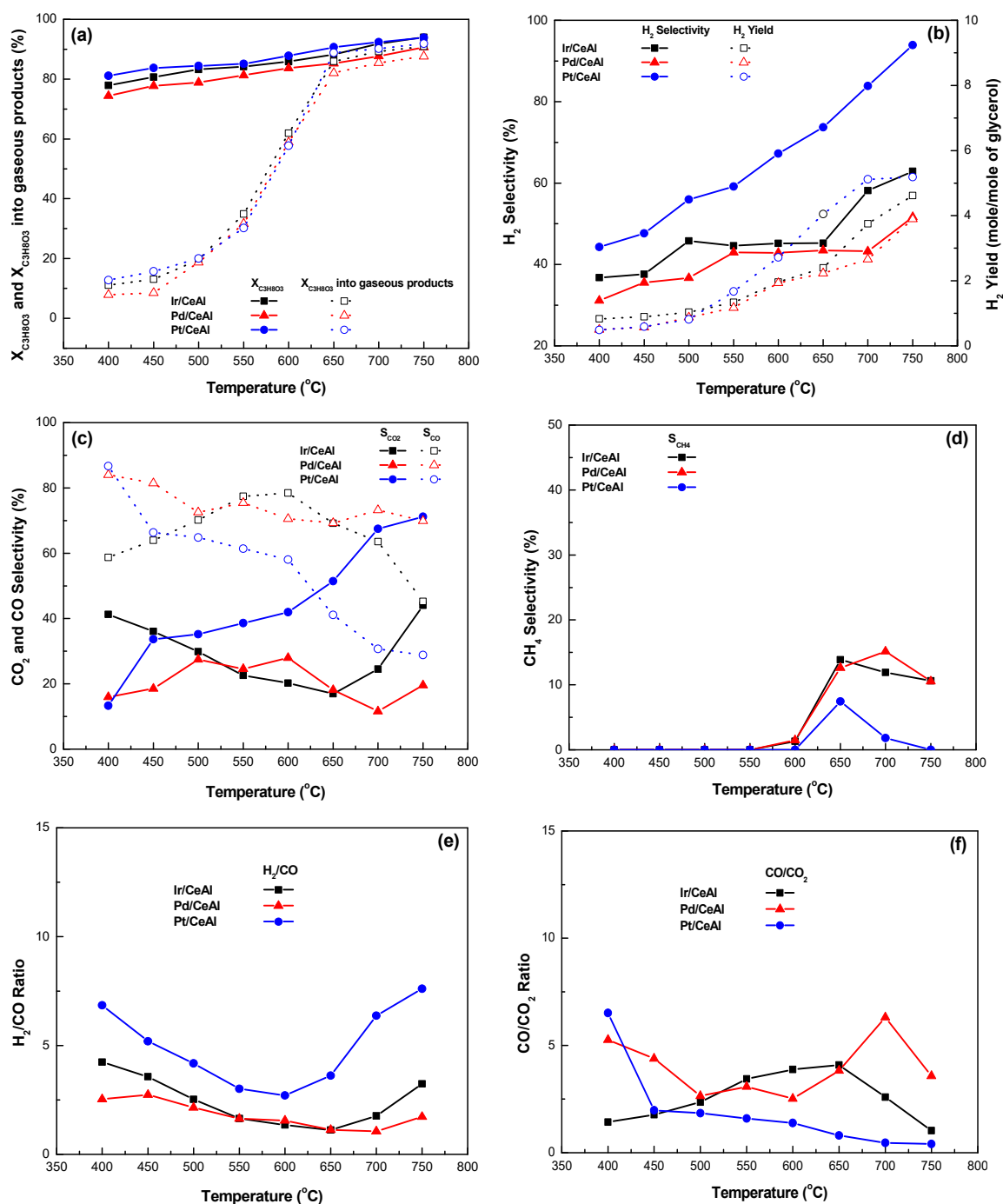


Figure 7. (a) Total $C_3H_8O_3$ conversion and $C_3H_8O_3$ conversion into gaseous products, (b) H_2 selectivity and yield, (c) CO_2 and CO selectivity, (d) CH_4 selectivity (y-axis on a different scale), (e) H_2/CO molar ratio, and (f) CO/CO_2 molar ratio (activity experiments).

From the results presented herein, and for all catalytic samples, it is obvious that the total conversion of $C_3H_8O_3$ is very high (above 75%) even at temperatures as low as 400 °C and reaches close to 95% over 650 °C (Figure 7a). On the other hand, temperature dramatically affects the conversion of $C_3H_8O_3$ into gaseous products, especially between 450 and 650 °C; over 650 °C $C_3H_8O_3$, gaseous almost reaches a plateau (Figure 7a). However, it is hard to discern any significant differences between the catalytic samples in terms of $C_3H_8O_3$ conversion. These results are explained by the endothermic nature of the GSR, which means that as the reaction temperature increases, the conversion of $C_3H_8O_3$ and the yield/selectivity to H_2 improve. At lower temperatures, the steam reforming reaction is limited,

as the water–gas-shift reaction is more dominant however, at higher temperatures, the active sites are able to cleave the C–C and/or C–O bonds in the $C_3H_8O_3$ molecules through dehydrogenation on the metal sites [30,92].

In terms of H_2 selectivity and yield (Figure 7b), the Pt/CeAl catalyst shows significantly higher H_2 selectivity in comparison to the other samples, with values starting at $\approx 44\%$ at $400\text{ }^\circ\text{C}$ and rising monotonically to $\approx 94\%$ at $750\text{ }^\circ\text{C}$. This is also reflected in the values recorded for H_2 yield, which rise from ≈ 0.5 ($400\text{ }^\circ\text{C}$) to ≈ 5.2 ($750\text{ }^\circ\text{C}$) H_2 mole/ $C_3H_8O_3$ mole. As mentioned above, according to thermodynamics, the maximum attainable H_2 yield is 6.2 [20]. Comparing the other two catalysts, it seems that the Ir/CeAl is slightly more selective to H_2 than the Pd/CeAl (for the Ir/CeAl, the S_{H_2} ranges from ≈ 37 to 63% and the Y_{H_2} from 0.8 to 4.6, from 400 to $750\text{ }^\circ\text{C}$, respectively). These results may indicate that the methanation reaction (at lower temperatures) and the RWGS reaction (at higher temperatures), both leading to the consumption of hydrogen, are more dominant on the Ir/CeAl and Pd/CeAl catalysts [93]. Moreover, the much improved performance of the Pt/CeAl may be related to: (i) the increased number of Brønsted acid sites (as shown by the TPD experiments), which improved the hydrogenolysis and dehydrogenation–dehydration of condensable intermediates, leading to enhanced H_2 production, and (ii) the smaller metal particle size (electron microscopy analysis), which favours the cleavage of the C–C and C–O bonds in the $C_3H_8O_3$ molecules. These findings are also in agreement with reports concerning the steam reforming of ethanol, which suggest that Pt-based catalysts exhibit higher activity and selectivity towards H_2 production in comparison to other noble metals [94,95].

Significant differences can be observed between the catalytic samples also in terms of S_{CO_2} and S_{CO} . Specifically, only the Pt/CeAl catalyst shows higher selectivity to CO_2 as the temperature rises (over $650\text{ }^\circ\text{C}$); in contrast for the Pd/CeAl, S_{CO} and S_{CO_2} remain almost steady despite the temperature increase (with S_{CO} significantly higher). As for the Ir/CeAl sample, despite progressively becoming more selective towards CO_2 as the temperature increases, it retains higher S_{CO} values for the entire temperature range. For example, at $650\text{ }^\circ\text{C}$, S_{CO_2} follows the order Pt/CeAl (52%) > Pd/CeAl (18%) > Ir/CeAl (17%), while S_{CO} is of the order Ir/CeAl \approx Pd/CeAl (69%) > Pt/CeAl (41%). These results show that the reverse water–gas-shift reaction probably dominates at high temperatures on the Pd and Ir catalysts; in contrast, its prevalence appears to diminish at high temperatures for the Pt/CeAl sample. Moreover, although CH_4 production is minimal between 400 – $600\text{ }^\circ\text{C}$ for all catalysts, it increases (albeit it still remains small) for the Ir/CeAl and Pd/CeAl catalysts over $650\text{ }^\circ\text{C}$, pointing to the occurrence of weak methanation activity over these two catalysts. The lack of CH_4 over the Pt/CeAl may be due to the occurrence of the methane steam reforming reaction, increasing H_2 and CO_2 production. The above observations are also reflected on the H_2/CO and CO/CO_2 ratios, which are higher and lower, respectively, for the Pt/CeAl catalyst in comparison to the other two samples.

For the work presented herein, a variety of liquid products in trace amounts were identified (e.g., propanal, phenol, 1-propanol, glycol aldehyde), but only the main effluents, i.e., acrolein, acetaldehyde, acetone, acetic acid, allyl alcohol and acetol, were quantified and the results are presented in Figure 8. As can be observed, the catalysts were selective towards the majority of the liquid products quantified between 400 and $500\text{ }^\circ\text{C}$ and appear only less selective towards acetic acid and acrolein. Over $500\text{ }^\circ\text{C}$ selectivity towards acetic acid increased for all samples, while that acrolein was eliminated. Notably, the Pt/CeAl sample stops producing liquid effluents over $650\text{ }^\circ\text{C}$ and the Pd/CeAl over $700\text{ }^\circ\text{C}$; in contrast, the Ir/CeAl produced allyl alcohol and acetic acid even at $750\text{ }^\circ\text{C}$.

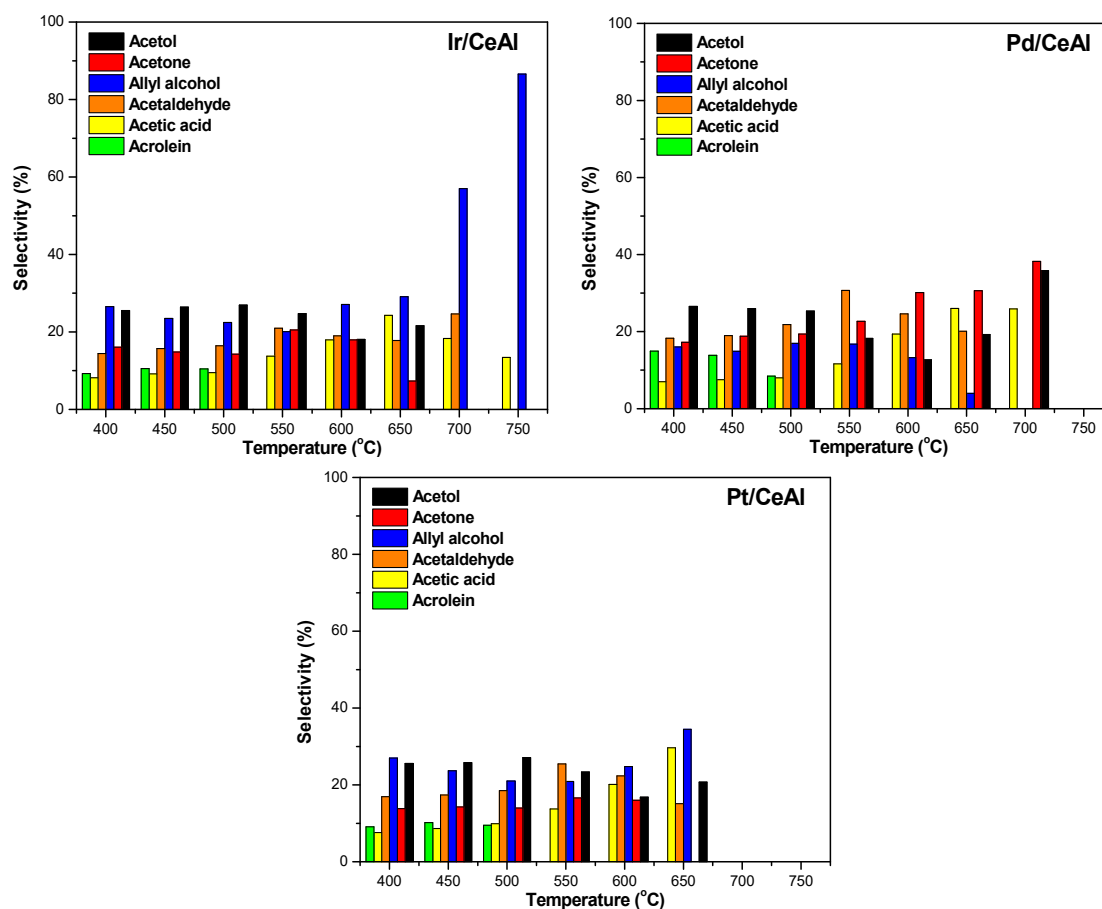


Figure 8. Selectivity of liquid phase products for the Ir/CeAl, Pd/CeAl and Pt/CeAl catalysts (activity experiments).

The reaction pathway that has been proposed [47] over the active metals and basic sites begins with the dehydrogenation of $C_3H_8O_3$, followed by a dehydration step leading to pyruvaldehyde, which may be converted to acetol (hydroxyacetone) through hydrogenation over the metallic sites and lactic acid, which may be produced by the Cannizzaro rearrangement due to the catalyst basicity. The decarbonylation of aldehyde from the cleavage of C–C bonds generates gaseous products. With regard to the acid–base properties, it is usually accepted that an important parameter is the balanced distribution of basic strength instead of only the strength of the acid sites. If this is not the case, the selectivity and the stability may be strongly affected [29,96]. However, there is a clear lack of fundamental studies regarding the basic properties in catalysed reactions (similar studies regarding the acid properties are much more developed) and much still needs to be done in order to get a better understanding of their effect on performance. Nonetheless, it is generally agreed that the strength of basic sites required for base-catalyzed reactions, or a base-catalyzed reaction step as in glycerol reforming, varies with the easiness of proton abstraction from the reactant molecule under the reaction conditions employed [97].

From the results presented herein, it seems likely that dehydrogenation and hydrogenolysis reactions led to the production of ethylene glycol, which was then converted to acetaldehyde and trace amounts of glycol aldehyde and ethanol (Route I). Hydroxyacetone (acetol) was probably produced through glycerol dehydration (Route II) and was then converted to form as main products acetic acid, acetone and acetaldehyde, and a variety of products in trace amounts, such as, 1,2-propanediol, propanal, 1-propanol, ethanol, formic acid, propionic acid, 2-cyclopentanone and phenol. This pathway is caused by the activation of the terminal –OH of glycerol on the Lewis acid sites, which is represented by the strong acid sites of the catalysts [98]. Glycerol dehydration also likely produced 3-hydroxypropanal

(Route III), which then formed allyl alcohol, acetaldehyde and acrolein as main products, and possibly formic acid and C_2H_4 (detected in trace amounts). This pathway involves the protonation of the secondary -OH of glycerol to form acrolein, which is favored by Brønsted acidity mainly represented by the moderate acid sites. A schematic representation of this plausible reaction pathway is been provided in Figure 9.

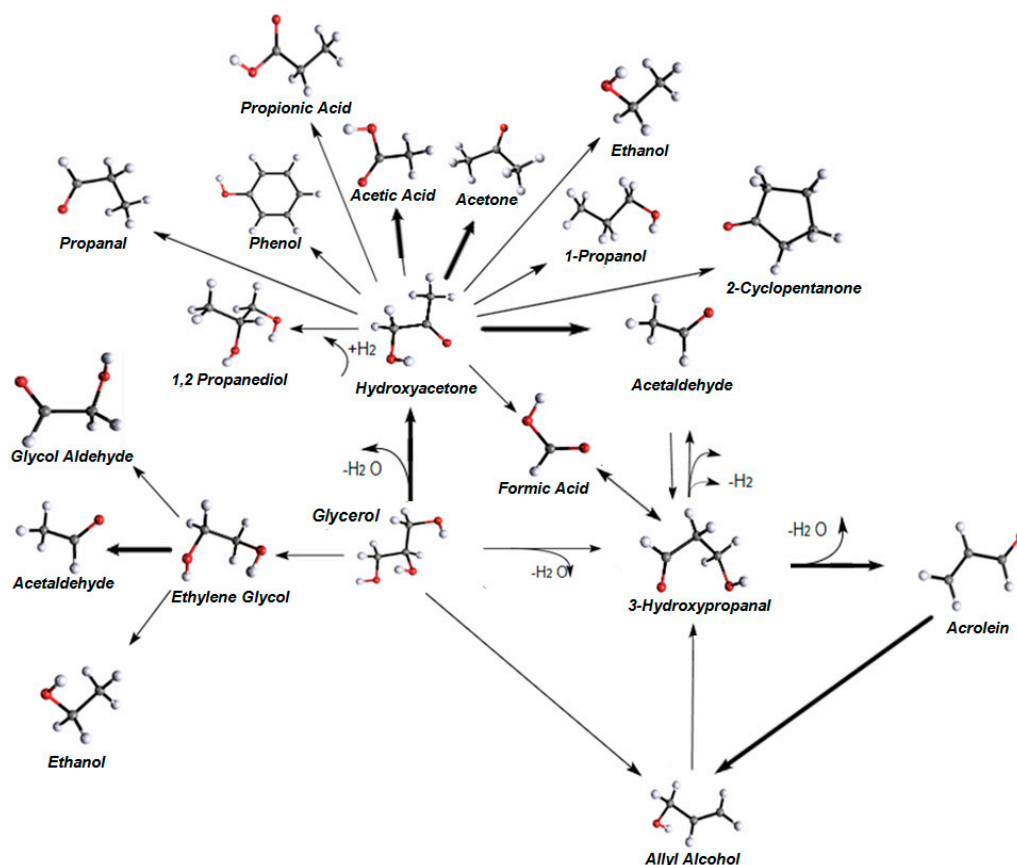


Figure 9. Schematic representation of the plausible reaction pathway for the glycerol steam reforming reaction.

It is noted that it is difficult to provide a direct comparison between the results presented herein and those reported by other authors in the literature due to differences in experimental conditions and catalyst systems under consideration. Buffoni et al. [45] examined the performance of 2 wt.% Pt catalysts supported on SiO₂ and SiO₂ composite for the GSR (liquid products were not analyzed); for the latter material, the authors reported an absence of surface acid sites and very small metallic particles (1.37 nm). After 2 h time-on-stream experiments carried out at 450 °C, at a WHSV = 25.7 h⁻¹ and a steam to carbon ratio (S/C) = 4, the Pt/SiO₂-C showed 70% total glycerol conversion, good selectivity towards H₂ (43%), high S_{CO} (81%), low S_{CO2} (13.8%) and low S_{CH4} (5.2%); H₂ yield was equal to 2.1. The relatively low H₂/CO (1.9) and high CO/CO₂ (4.0) ratios can probably be explained by an increased contribution from the RWGS reaction. De Rezende et al. [47] prepared layered double hydroxides containing Mg and Al to support 1 wt.% Pt catalysts. For the experimental work, the authors used a WGFR = 9:1 (molar), contact time of 511 h⁻¹ and reported, at reaction temperature of 600 °C, relatively high S_{H2} (from 48.5 to 68.2% depending on the specific sample) and S_{CO2} (50.0–59.5%) and low to moderate S_{CO} (9.7–27.0%); the main liquid products obtained were acetol, piruvadehyde, lactic acid, acetic acid, acetaldehyde and formic acid. Pompeo et al. [49] compared the performance of Pt (1 and 2 wt.%) and Ni (5 wt.%) catalysts supported on SiO₂ at temperatures between 350 and 450 °C, using 10 wt.% of glycerol in the feed. The authors, using a very low WHSV (from 0.44 to 1.66 min⁻¹) reported that the

1Pt catalyst showed 75% $C_3H_8O_3$ conversion at 350 °C (84% for the 2Pt catalyst) and 100% $X_{C_3H_8O_3}$ at 450 °C; the major liquid products identified were acetaldehyde, 2-oxopropanal, hydroxy-acetaldehyde, 1-hydroxy-2-propanone, 1,2-ethanediol, 1,3-dihydroxy-2-propanone, and 2,3-dihydroxy-propanal. Zhang et al. [56] used an Ir/CeO₂ catalyst (2 wt.% Ir) and a high WGFR (2 vol%) and showed $X_{C_3H_8O_3}$ of 100% and $S_{H_2} = 85\%$ at 400 °C at a gas hourly space velocity of 11,000 mL g_{cat}^{−1} h^{−1}; liquid products were not analyzed. Ebshish et al. [58] compared the performance of Ce/Al₂O₃ (1–10 wt.% Ce) and Pd/Al₂O₃ catalysts (1 wt.% Pd), at 600 °C using a WGFR = 6:1 (molar) and reported that the highest Y_{H_2} was achieved by the noble metal catalyst (3.92 mole of H₂ per mole of $C_3H_8O_3$); the authors attributed the good performance of the Pd catalyst to favourable lattice parameters.

2.3. Catalytic Stability

Figure 10 presents the results obtained during the time-on-stream experiments, which were undertaken at 600 °C but at lower WGFR (9:1, molar) in comparison to the activity tests, i.e., the conditions chosen for the stability tests were more severe, in an effort to induce catalyst deactivation.

As can be observed from Figure 10a, all catalysts experience a loss in their ability to convert glycerol during the first few hours of the experiments, but after approximately 4 h the values recorded are rather stable. Although the $X_{C_3H_8O_3}$ is high for all catalysts, it dropped from 90% (1st measurement) to 79% (8th h) for the Ir/CeAl sample, from 89% (1st measurement) to 75% (8th h) for the Pd/CeAl, and from 93% (1st measurement) to 81% (8th h) for the Pt/CeAl. The loss in the ability to convert $C_3H_8O_3$ to gaseous products was more pronounced, dropping from 29% to 11% for the Ir/CeAl, 42% to 11% for the Pd/CeAl and 44% to 15% for the Pt/CeAl catalyst, between the first and last measurements, respectively. However, all catalysts retain high and rather stable S_{H_2} (Figure 10b) with the Pt/CeAl clearly being more selective. In contrast, the Y_{H_2} is low for all catalysts with the values recorded at the end of the stability tests approximately 0.5 for the Ir and Pd and 1.0 for the Pt catalyst. Moreover, as the experiments progress, the Ir and Pd catalysts become progressively more selective to CO and less selective to CO₂; only the Pt catalyst retains rather stable S_{CO} and S_{CO_2} values. These observations are also reflected when examining the H₂/CO and CO/CO₂ ratios (Figure 10e,f, respectively). Finally, CH₄ production was non-existent for all catalytic samples (Figure 10d). In terms of liquid products (not shown herein), all catalysts retained rather stable selectivity values for the duration of the experiment. These results indicate that the RWGS reaction, consuming H₂ and producing CO, was the dominant reaction at the temperature the experiments were undertaken.

In an excellent study, Wang et al. [99] performed a series of ageing experiments on an Ir/CeO₂ catalyst for the steam reforming of ethanol. The authors reported fast initial deactivation, followed by a levelling of performance with time, and were able to show that a significant loss of surface area and microporosity occurred when CeO₂ came into contact with steam; sintering and carbon deposition occurred at a more gradual pace. In relation to the GSR, De Rezende et al. [47] reported very quick deactivation for a series of PtMgAl-H (H for hydroxide), with the PtMg3Al-H showing a drop from 80% to 20% in $X_{C_3H_8O_3}$ during 250 min of time-on-stream carried out at 600 °C. $X_{C_3H_8O_3, \text{gaseous}}$ was also low, dropping from ≈45% to 25%. Similarly to the results reported herein, they also observed that the selectivity to liquid products was stable during time-on-stream. Using TPO and TEM experiments, the authors argued that the main cause for catalyst deactivation was carbon deposition. Buffoni et al. [45] also reported sharp deactivation for Pt/SiO₂ and Pt/C catalysts during time-on-stream; only the Pt/SiO₂-C catalyst retained stable $X_{C_3H_8O_3}$ values throughout, losing only 10% of its initial activity after 66 h of time-on-stream. Moreover, the H₂ yield of the Pt/SiO₂ was approximately 1.5 at the end of the experiment. The authors, using TGA/TPO, Raman and XPS, were able to show that the cause of deactivation was carbon deposition and sintering of the metallic particles. Similarly, Sad et al. [46] also reported decreased conversion of glycerol to gas products over time for Pt catalysts on different supports (SiO₂, MgO, Al₂O₃, TiO₂), which was larger by an order of magnitude for the more acidic supports.

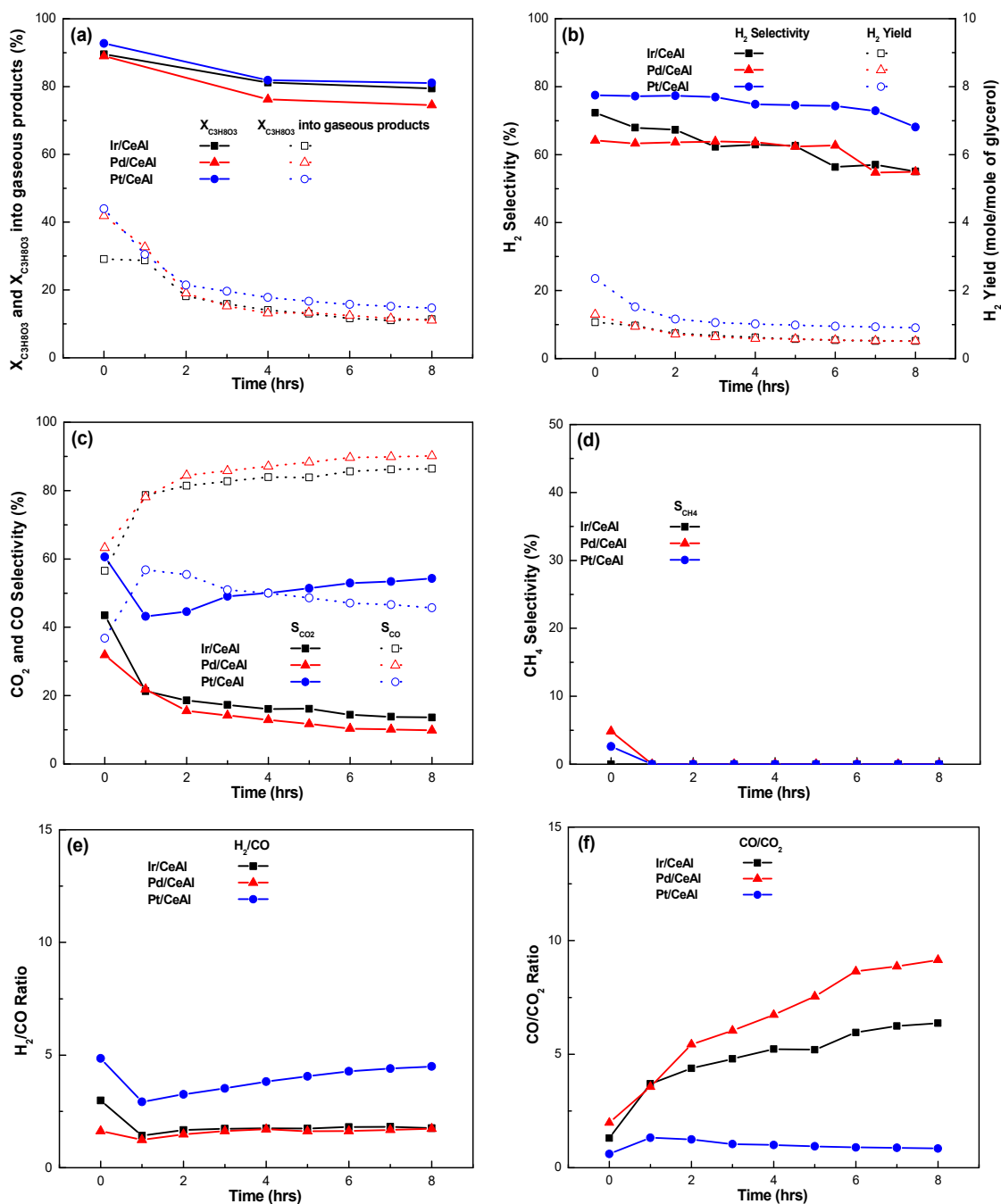


Figure 10. Time-on-stream experiments for all catalysts: (a) Total $C_3H_8O_3$ conversion and $C_3H_8O_3$ conversion into gaseous products, (b) H_2 selectivity and yield, (c) CO_2 , CO selectivity (y-axis on a different scale), (d) CH_4 selectivity (y-axis on a different scale), (e) H_2/CO molar ratio, (f) CO/CO_2 molar ratio.

Figure 11 shows the TEM images and particle size distribution histograms obtained for the spent Ir/CeAl (Figure 11a), Pd/CeAl (Figure 11b) and Pt/CeAl (Figure 11c) catalysts, after the time-on-stream experiments. The improved resistance to sintering was shown by the Pt/CeAl catalyst, as the average particle size was 1.7 ± 3.0 nm, quite close to that calculated for the reduced equivalent (1.1 ± 0.2 nm), due to the stronger interaction of Pt with the $CeO_2-Al_2O_3$ support (TPR measurements). The effect of sintering was also rather limited on the Pd/CeAl catalyst, as the average particle size was found to be 5.2 ± 1.9 nm (3.7 ± 2.0 nm for the reduced sample). However, the weak interaction of Ir with the support—which may have resulted from the high calcination temperature (800 °C) used herein—led

to extensive sintering of the Ir particles and a multimodal particle size distribution, with a mean particle size value of 12.3 ± 4 (1.6 ± 0.4 nm for the reduced sample) and 62.6 ± 32.7 nm (11.8 ± 6.6 nm for the reduced sample), thereby the number of active sites available to the reactants was greatly reduced. A similar observation, i.e., extensive Ir sintering when high calcination temperatures were used, was also made by Zou et al. [100] for Ir/CeO₂ catalysts tested for the steam reforming of ethanol. These large particles in turn led to the formation of fibrous carbon deposits, as can be clearly observed from the images presented herein. In contrast, for the Pd and Pt catalysts, the coke deposited during the stability tests appears mainly amorphous. Carbon nanotubes, on spent Ir catalysts, were also observed in the works of Wang et al. [99] and Zou et al. [100]. As is well understood, carbon deposition is a major issue for the GSR as it can occur over a variety of routes e.g., dehydration over the metallic oxides leading to the formation of unsaturated hydrocarbon species or cracking of intermediates on the catalysts' surface [47].

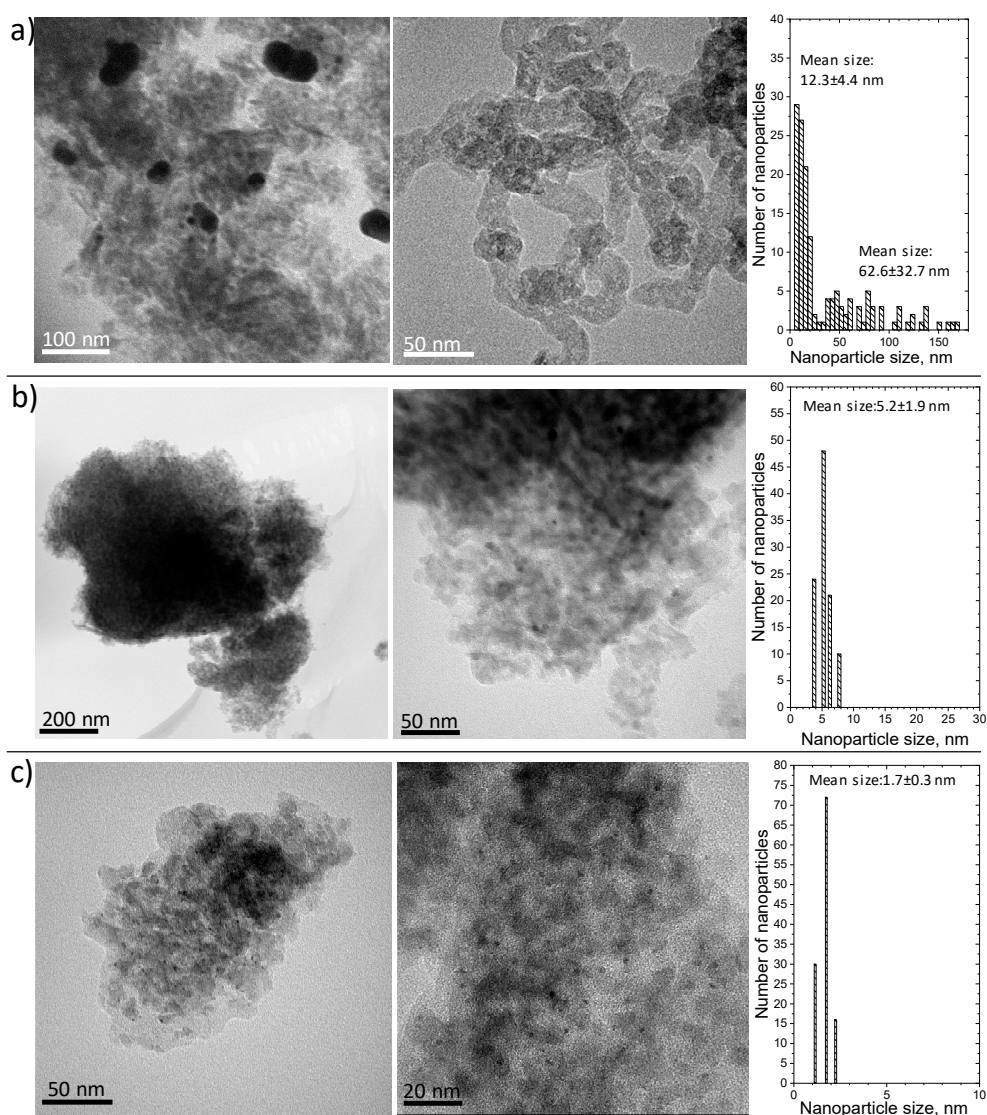


Figure 11. TEM images and particle size distribution of the spent: (a) Ir/CeAl, (b) Pd/CeAl, and (c) Pt/CeAl catalysts.

3. Materials and Methods

3.1. Catalyst Preparation

The alumina support used herein was purchased from Akzo and was crashed and sieved to 350–500 μm , as it was in pellet form. This was followed by calcination, which was carried out at 800 $^{\circ}\text{C}$ for 4 h, in ambient air. The $\text{CeO}_2\text{--Al}_2\text{O}_3$ support was prepared by the incipient wetness impregnation technique using $\text{Ce}(\text{NO}_3)_3 \cdot 6\text{H}_2\text{O}$ (99.95%) aqueous solutions (Sigma Aldrich, St Luis, MS, USA), with a defined concentration of CeO_2 and a volume equal to the total pore volume of the impregnated Al_2O_3 , in order to obtain a nominal loading of 10 wt.% CeO_2 in the final support. After the impregnation, the support was dried in ambient air at 120 $^{\circ}\text{C}$ for 12 h followed by calcination in ambient air at 600 $^{\circ}\text{C}$ for 5 h. The incipient wetness impregnation method was also employed for the incorporation of the Pt, Pd and Ir active phases into the 10% $\text{CeO}_2\text{--Al}_2\text{O}_3$ support using $\text{Pt}(\text{NH}_3)_4(\text{NO}_3)_2$, $\text{IrCl}_3\text{H}_2\text{O}$ and PdCl_2 precursors (Sigma Aldrich). The derived catalytic samples were dried in ambient air at 120 $^{\circ}\text{C}$ overnight and finally calcined at 600 $^{\circ}\text{C}$ in ambient air for 5 h (these samples are denoted throughout this manuscript as calcined catalysts). Reduced counterparts were also produced by in situ reduction for 1 h at 800 $^{\circ}\text{C}$ in pure H_2 flow (denoted as reduced catalysts). The catalysts are labelled as Ir/CeAl, Pd/CeAl and Pt/CeAl.

3.2. Catalyst Characterization

The specific surface area, pore volume and pore size distribution of the catalysts were studied using a high-resolution 3Flex Micromeritics (Atlanta, GA, USA) porosimeter. The catalysts' crystalline structure was determined by applying the X-ray diffraction (XRD) technique, using a ThermoAl diffractometer (Waltham, MA, USA) at 40 kV and 30 mA with $\text{Cu K}\alpha$ radiation ($\lambda = 0.154178\text{ nm}$). Diffractograms were recorded in the $2\theta = 2\text{--}70^{\circ}$ range at a scanning rate of 0.04° over 1.2 min^{-1} . The reduction behavior and the Ni-support interaction were probed using H_2 titration and a temperature-programmed reduction technique ($\text{H}_2\text{--TPR}$), whereas the acidity/basicity of the catalysts was monitored using a temperature-programmed desorption ($\text{NH}_3\text{--}/\text{CO}_2\text{--TPD}$) experiments (Autochem 2920, Micromeritics, Atlanta, GA, USA) unit. Surface studies in terms of oxidation state and atomic surface composition were performed using X-ray Photoelectron Spectroscopy (XPS), carried out on a ThermoFisher Scientific Instruments (East Grinstead, UK) K-Alpha+ spectrometer using a monochromated $\text{Al K}\alpha$ X-ray source ($h\nu = 1486.6\text{ eV}$). Charges on the surface were neutralized using low energy electrons and argon ions in order to have a C 1s binding energy for adventitious carbon of 284.8 eV. The spectra were fitted using CasaXPS (v2.3.17 PR1.1) and Scofield sensitivity factors with an energy exponent of -0.6 . Energy dispersive X-ray spectroscopy (EDS) and high angle annular dark field scanning transmission electron microscopy (STEM-HAADF) were performed on a Tecnai G2-F30 Field Emission Gun microscope (Waltham, MA, USA) with a super-twin lens and 0.2 nm point-to-point resolution and 0.1 nm line resolution operated at 300.

3.3. Catalytic Tests

The GSR was carried out at atmospheric pressure, using a continuous flow fixed-bed reactor. A detailed description of the experimental set up can be found in previous publications by our group [2]. In synopsis, the work carried out herein necessitated the use of both liquid and gaseous streams as feeds, and for this reason the experimental rig consisted of two vaporizers and a pre-heater before the reactor and a condenser after it. The vaporizers, pre-heater and reactor were placed into electrical ovens and regulated with programmed-temperature controllers. The gases at the outlet were forced through a cold trap in order to capture the liquid products. The glycerol used had 99.5% purity and was supplied by Sigma Aldrich. Catalytic activation was carried out in situ (prior to catalytic testing), under a flow (100 Nml min^{-1}) of high purity H_2 (5.0) at 800 $^{\circ}\text{C}$ for 1h.

The activity and selectivity of the catalytic samples was examined in the temperature range of 40 $^{\circ}\text{C}$ (activity experiments) using an aqueous solution of 0.12 Nml min^{-1} (20 v.v.% $\text{C}_3\text{H}_8\text{O}_3$ in H_2O)

and a gas stream of 38 NmL min⁻¹ of He (99.999%). Thus, the gas mixture at inlet of the reactor consisted of: 73% H₂O, 4% C₃H₈O₃ and 23% He. This corresponded to Weight Hourly Space Velocity (WHSV) equal to 50,000 NmL g⁻¹ h⁻¹. Catalytic stability (time-on-stream experiments) was assessed at 600 °C using a higher concentration of glycerol in the liquid stream, set at 31 v.v.% C₃H₈O₃ (63% H₂O, 7% C₃H₈O₃, 30% He), but the WHSV was kept at 50,000 NmL g⁻¹ h⁻¹. These experiments were carried out for 8 h and gaseous products were measured every hour and liquid products every 4 h.

The liquid products were analysed via a combination of Gas Chromatography (Agilent 7890A) and Mass Spectroscopy (Agilent 5975C). The gaseous products were determined via an Agilent gas chromatographer (7890A). Detailed information regarding the analysis of liquid and gaseous products can be found at ref. [19].

3.4. Reaction Metrics

The investigation of catalytic performance necessitated the calculation of the total glycerol conversion, the conversion of glycerol into gaseous products, and the determination of the H₂ yield and selectivities to H₂, CH₄, CO₂ and CO. For the calculations, Equations (13)–(17) shown below were used. The selectivity to acetone [(CH₃)₂CO], acetaldehyde (C₂H₄O), acetol (C₃H₆O₂), allyl alcohol (CH₂=CHCH₂OH), acrolein (C₃H₄O) and acetic acid (C₂H₄O) was calculated based on Equation (18):

$$\% \text{Glycerol conversion}_{(\text{total conversion})} = \left(\frac{\text{Glycerol}_{\text{in}} - \text{Glycerol}_{\text{out}}}{\text{Glycerol}_{\text{in}}} \right) \times 100 \quad (13)$$

$$\% \text{Glycerol conversion}_{(\text{gaseous products})} = \left(\frac{\text{C atoms in the gas products}}{\text{total C atoms in the feedstock}} \right) \times 100 \quad (14)$$

$$\text{H}_2 \text{ yield} = \frac{\text{H}_2 \text{ mol produced}}{\text{mol of glycerol in the feedstock}} \quad (15)$$

$$\% \text{H}_2 \text{ selectivity} = \left(\frac{\text{H}_2 \text{ mol produced}}{\text{C atoms produced in the gas phase}} \right) \times \left(\frac{1}{\text{RR}} \right) \times 100 \quad (16)$$

$$\% \text{ Selectivity of } i = \left(\frac{\text{C atoms in species } i}{\text{C atoms produced in the gas phase}} \right) \times 100 \quad (17)$$

$$\% \text{ Selectivity of } i' = \left(\frac{\text{C atoms in species } i'}{\text{C atoms produced in the liquid phase}} \right) \times 100 \quad (18)$$

where, RR is defined as the ratio of mol of H₂ to CO₂ formed, i.e., the reforming ratio (7/3), species *i* refers to CO₂, CO and CH₄ and species *i'* refers to acetol, acetone, allyl alcohol, acetaldehyde, acrolein and acetic acid.

4. Conclusions

The rapid development of the biodiesel industry means that the utilization of its main by-product, i.e., glycerol is a matter that needs to be urgently resolved. An attractive possibility is provided by glycerol's energetic valorisation via the steam reforming reaction for the production of H₂, an efficient energy carrier that can provide clean power in stationary, portable and transport applications. In the work presented herein, Al₂O₃ and CeO₂-Al₂O₃ (10 wt.%) were used as supporting material for Ir, Pd and Pt catalysts, which were prepared by the incipient wetness impregnation technique; calcination was carried out in ambient air at 800 °C, while activation was carried out in situ under a pure H₂ flow, also at 800 °C. The catalysts were characterised using N₂ adsorption-desorption, XRD, TPR, TPD, XPS and TEM analysis. The catalytic experiments aimed at identifying the effect of temperature on the total conversion of glycerol, on the conversion of glycerol to gaseous products, the selectivity towards the gaseous products (H₂, CO₂, CO, CH₄) and the determination of the H₂/CO and CO/CO₂ molar ratios. The main liquid effluents produced during the reaction were quantified. Time-on-stream experiments

were conducted for 8h at harsh reaction conditions in order to induce catalyst deactivation. The results revealed that the Pt/CeAl catalyst was more selective towards H₂, which can be related to its increased number of Brønsted acid sites, which improved the hydrogenolysis and dehydrogenation–dehydration of condensable intermediates. The time-on-stream experiments, undertaken at low Water–Glycerol Feed Ratios (WGFR), showed gradual deactivation for all catalysts. This is likely due to the dehydration reaction, which leads to the formation of unsaturated hydrocarbon species and eventually to carbon deposition. The weak metal–support interaction shown for the Ir/CeAl catalyst also led to pronounced sintering of the metallic particles.

Author Contributions: Conceptualization, N.D.C. and M.A.G.; Data curation, N.D.C., G.I.S., K.N.P., D.M., V.S., K.P. and M.A.G.; Formal analysis, N.D.C., K.N.P. and M.A.G.; Funding acquisition, M.A.G.; Investigation, N.D.C., G.I.S. and K.N.P.; Methodology, N.D.C. and M.A.G.; Project administration, N.D.C. and M.A.G.; Supervision, N.D.C.; Validation, N.D.C. and M.A.G.; Writing—original draft, N.D.C., G.I.S. and K.N.P.; Writing—review & editing, N.D.C., N.D., K.N.P. and M.A.G. All authors have read and agreed to the published version of the manuscript.

Funding: N.D.C., G.I.S. and M.A.G. are grateful to the Research Committee of the University of Western Macedonia for financial support through grant no. 70304. K.N.P. acknowledges the financial support from the Abu Dhabi Department of Education and Knowledge (ADEK) under the AARE 2019-233 grant and support by the Khalifa University of Science and Technology under Award No. RC2-2018-024.

Conflicts of Interest: The authors declare no conflict of interest.

References

- Zalasiewicz, J.; Waters, C.N.; Summerhayes, C.P.; Wolfe, A.P.; Barnosky, A.D.; Cearreta, A.; Crutzen, P.; Ellis, E.; Fairchild, I.J.; Gałuszka, A.; et al. The Working Group on the Anthropocene: Summary of evidence and interim recommendations. *Anthropocene* **2017**, *19*, 55–60. [\[CrossRef\]](#)
- Douvartzides, S.L.; Charisiou, N.D.; Papageridis, K.N.; Goula, M.A. Green Diesel: Biomass Feedstocks, Production Technologies, Catalytic Research, Fuel Properties and Performance in Compression Ignition Internal Combustion Engines. *Energies* **2019**, *12*, 809. [\[CrossRef\]](#)
- Jin, W.; Pastor-Pérez, L.; Villora-Pico, J.J.; Pastor-Blas, M.M.; Sepúlveda-Escribano, A.; Gu, S.; Charisiou, N.D.; Papageridis, K.; Goula, M.A.; Reina, T.R. Catalytic conversion of palm oil to bio-hydrogenated diesel over novel N-doped activated carbon supported Pt nanoparticles. *Energies* **2019**, *13*, 132. [\[CrossRef\]](#)
- Ibarra-Gonzalez, P.; Rong, B.G. A review of the current state of biofuels production from lignocellulosic biomass using thermochemical conversion routes. *Chin. J. Chem. Eng.* **2019**, *27*, 1523–1535. [\[CrossRef\]](#)
- Charisiou, N.D.; Polychronopoulou, K.; Asif, A.; Goula, M.A. The potential of glycerol and phenol towards H₂ production using steam reforming reaction: A review. *Surf. Coat. Technol.* **2018**, *352*, 92–111. [\[CrossRef\]](#)
- Manaf, I.S.A.; Embong, N.H.; Hhazaai, S.N.M.; Rahim, M.H.A.; Yusoff, M.M.; Lee, K.T.; Maniam, G.P. A review for key challenges of the development of biodiesel industry. *Energy Convers. Manag.* **2019**, *185*, 508–517. [\[CrossRef\]](#)
- Goula, M.A.; Charisiou, N.D.; Pandis, P.K.; Stathopoulos, V.N. Ni/apatite-type lanthanum silicate supported catalyst for the glycerol steam reforming reaction. *RCS Advan.* **2016**, *6*, 78954–78958. [\[CrossRef\]](#)
- Polychronopoulou, K.; Charisiou, N.D.; Papageridis, K.N.; Sebastian, V.; Dabbawala, A.A.; AlKhoori, A.A.; Goula, M.A. The effect of Ni addition onto a Cu-based ternary support on the H₂ production over glycerol steam reforming reaction. *Nanomaterials* **2018**, *8*, 931. [\[CrossRef\]](#)
- Bagheri, S.; Julkapli, N.M.; Yehye, W.A. Catalytic conversion of biodiesel derived raw glycerol to value added products. *Renew. Sust. Energ. Rev.* **2015**, *41*, 113–127. [\[CrossRef\]](#)
- Jiang, B.; Li, L.; Bian, Z.; Li, Z.; Sun, Z.; Tang, D.; Kawi, S.; Dou, B.; Goula, M.A. Chemical looping glycerol reforming for hydrogen production by Ni@ZrO₂ nano-composite oxygen carriers. *Int. J. Hydrog. Energ.* **2018**, *43*, 13200–13211. [\[CrossRef\]](#)
- Charisiou, N.D.; Papageridis, K.N.; Siakavelas, G.; Tzounis, L.; Goula, M.A. Effect of active metal supported on SiO₂ for selective hydrogen production from the glycerol steam reforming reaction. *BioResources* **2016**, *11*, 10173–10189. [\[CrossRef\]](#)
- Ayodele, B.M.; Abdullah, T.A.R.B.T.; Alsaffar, M.A.; Mustapa, S.I.; Salleh, S.F. Recent advances in renewable hydrogen production by thermo-catalytic conversion of biomass-derived glycerol: Overview of prospects and challenges. *Int. J. Hydrog. Energ.* **2020**, *45*, 18160–18185. [\[CrossRef\]](#)

13. Polychronopoulou, K.; Charisiou, N.D.; Siakavelas, G.; AlKhoori, A.A.; Sebastian, V.; Hinder, S.J.; Baker, M.A.; Goula, M.A. Ce–Sm–xCu cost efficient catalysts for H₂ production through the glycerol steam reforming reaction. *Sust. Energ. Fuels* **2019**, *3*, 673–691. [\[CrossRef\]](#)
14. Dou, B.; Zhang, H.; Cui, G.; He, M.; Chen, H.; Xu, Y.; Wu, C. Hydrogen sorption and desorption behaviors of Mg–Ni–Cu doped carbon nanotubes at high temperature. *Energy* **2019**, *167*, 1097–1106. [\[CrossRef\]](#)
15. Goula, M.A.; Charisiou, N.D.; Papageridis, K.N.; Delimitis, A.; Pachatouridou, E.; Iliopoulou, E.F. Nickel on alumina catalysts for the production of hydrogen rich mixtures via the biogas dry reforming reaction: Influence of the synthesis method. *Int. J. Hydrog. Energ.* **2015**, *40*, 9183–9200. [\[CrossRef\]](#)
16. Bepari, S.; Pradham, N.C.; Dalai, A. Selective production of hydrogen by steam reforming of glycerol over Ni/Fly ash catalyst. *Catal. Today* **2017**, *291*, 36–46. [\[CrossRef\]](#)
17. Charisiou, N.D.; Siakavelas, G.; Papageridis, K.N.; Sebastian, V.; Hinder, S.J.; Baker, M.A.; Polychronopoulou, K.; Goula, M.A. The influence of SiO₂ doping on the Ni/ZrO₂ supported catalyst for hydrogen production through the glycerol steam reforming reaction. *Catal. Today* **2019**, *319*, 206–219. [\[CrossRef\]](#)
18. Saidi, M.; Moradi, P. Conversion of biodiesel synthesis waste to hydrogen in membrane reactor: Theoretical study of glycerol steam reforming. *Int. J. Hydrog. Energ.* **2020**, *45*, 8715–8726. [\[CrossRef\]](#)
19. Papageridis, K.N.; Charisiou, N.D.; Siakavelas, G.; Avraam, D.G.; Tzounis, L.; Kousi, K.; Goula, M.A. Comparative study of Ni, Co, Cu supported on γ -alumina catalysts for hydrogen production via the glycerol steam reforming reaction. *Fuel Proc. Technol.* **2016**, *152*, 156–175. [\[CrossRef\]](#)
20. Adhikari, S.; Fernando, S.; Gwaltney, S.R.; To, S.D.F.; Bricka, R.M.; Steele, P.H.; Haryanto, A. A thermodynamic analysis of hydrogen production by steam reforming of glycerol. *Int. J. Hydrogen. Energ.* **2007**, *32*, 2875–2880. [\[CrossRef\]](#)
21. Goula, M.A.; Charisiou, N.D.; Papageridis, K.N.; Siakavelas, G. Influence of the synthesis method parameters used to prepare nickel-based catalysts on the catalytic performance for the glycerol steam reforming reaction. *Chin. J. Catal.* **2016**, *37*, 1949–1965. [\[CrossRef\]](#)
22. Dahdah, E.; Estephane, J.; Gennequin, C.; Aboukais, A.; Abi-Aad, E.; Aouad, S. Zirconia supported nickel catalysts for glycerol steam reforming: Effect of zirconia structure on the catalytic performance. *Int. J. Hydrogen Energy* **2020**, *45*, 4457–4467. [\[CrossRef\]](#)
23. Dou, B.; Song, Y.; Wang, C.; Chen, H.; Xu, Y. Hydrogen production from catalytic steam reforming of biodiesel byproduct glycerol: Issues and challenges. *Renew. Sust. Energ. Rev.* **2014**, *30*, 950–960. [\[CrossRef\]](#)
24. Silva, J.M.; Soria, M.; Madeira, L.M. Thermodynamic analysis of glycerol steam reforming for hydrogen production with in situ hydrogen and carbon dioxide separation. *J. Power Sources* **2015**, *273*, 423–430. [\[CrossRef\]](#)
25. Charisiou, N.D.; Sebastian, V.; Hinder, S.J.; Baker, M.A.; Polychronopoulou, K.; Goula, M.A. Ni catalysts based on attapulgite for hydrogen production through the glycerol steam reforming reaction. *Catalysts* **2019**, *9*, 650. [\[CrossRef\]](#)
26. Da Menezes, S.Q.J.P.; Manfro, R.L.; Souza, M.M.V.M. Hydrogen production from glycerol steam reforming over nickel catalysts supported on alumina and niobia: Deactivation process, effect of reaction conditions and kinetic modeling. *Int. J. Hydrogen Energy* **2018**, *43*, 15064–15082. [\[CrossRef\]](#)
27. Charisiou, N.D.; Siakavelas, G.; Tzounis, L.; Dou, B.; Sebastian, V.; Hinder, S.J.; Baker, M.A.; Polychronopoulou, K.; Goula, M.A. Ni/Y₂O₃–ZrO₂ catalyst for hydrogen production through the glycerol steam reforming reaction. *Int. J. Hydrogen Energy* **2020**, *45*, 10442–10460. [\[CrossRef\]](#)
28. Charisiou, N.D.; Siakavelas, G.; Sebastian, V.; Baker, M.A.; Hinder, S.J.; Polychronopoulou, K.; Goula, M.A. Hydrogen production from the steam reforming of glycerol over Ni catalysts supported on Al₂O₃ and AlCeO₃. *Catalysts* **2019**, *9*, 411. [\[CrossRef\]](#)
29. Charisiou, N.D.; Papageridis, K.N.; Siakavelas, S.; Tzounis, L.; Kousi, K.; Baker, M.A.; Hinder, S.J.; Sebastian, V.; Polychronopoulou, K.; Goula, M.A. Glycerol steam reforming for hydrogen production over nickel supported on alumina, zirconia and silica catalysts. *Top. Catal.* **2017**, *60*, 1226–1250. [\[CrossRef\]](#)
30. Charisiou, N.D.; Papageridis, K.N.; Tzounis, L.; Sebastian, V.; Baker, M.A.; Hinder, S.J.; AlKetbi, M.; Polychronopoulou, K.; Goula, M.A. Ni supported on CaO–MgO–Al₂O₃ as a highly selective and stable catalyst for H₂ production via the glycerol steam reforming reaction. *Int. J. Hydrogen Energy* **2019**, *44*, 256–273. [\[CrossRef\]](#)

31. Charisiou, N.D.; Siakavelas, G.; Papageridis, K.N.; Baklavaridis, A.; Tzounis, L.; Polychronopoulou, K.; Goula, M.A. Hydrogen production via the glycerol steam reforming reaction over nickel supported on alumina and lanthana–alumina catalysts. *Int. J. Hydrogen Energy* **2017**, *42*, 13039–13060. [\[CrossRef\]](#)
32. Yancheshmeh, M.S.; Sahraei, O.A.; Aissaoui, M.; Iliuta, M.C. A novel synthesis of NiAl_2O_4 spinel from a Ni–Al mixed–metal alkoxide as a highly efficient catalyst for hydrogen production by glycerol steam reforming. *Appl. Catal. B Environ.* **2020**, *265*, 118535. [\[CrossRef\]](#)
33. Chen, D.; Wang, W.; Liu, C. Hydrogen production through glycerol steam reforming over beehive–biomimetic graphene–encapsulated nickel catalysts. *Renew. Energy* **2020**, *145*, 2647–2657. [\[CrossRef\]](#)
34. Wang, B.; Xiong, Y.; Han, Y.; Hong, J.; Zhang, Y.; Li, J.; Jing, F.; Chu, W. Preparation of stable and highly active Ni/CeO₂ catalysts by glow discharge plasma technique for glycerol steam reforming. *Appl. Catal. B Environ.* **2019**, *249*, 257–265. [\[CrossRef\]](#)
35. Veiga, S.; Faccio, R.; Romero, M.; Bussi, J. Utilization of waste crude glycerol for hydrogen production via steam reforming over Ni–La–Zr catalysts. *Biomass Bioenerg.* **2020**, *135*, 105508. [\[CrossRef\]](#)
36. Lima, D.S.; Calgaro, C.O.; Perez-Lopez, O.W. Hydrogen production by glycerol steam reforming over Ni based catalysts prepared by different methods. *Biomass Bioenerg.* **2019**, *130*, 105358. [\[CrossRef\]](#)
37. Charisiou, N.D.; Douvartzides, S.L.; Siakavelas, G.I.; Tzounis, L.; Sebastian, V.; Stolojan, V.; Hinder, S.J.; Baker, M.A.; Polychronopoulou, K.; Goula, M.A. The relationship between reaction temperature and carbon deposition on nickel catalysts based on Al₂O₃, ZrO₂ or SiO₂ supports during the biogas dry reforming reaction. *Catalysts* **2019**, *9*, 676. [\[CrossRef\]](#)
38. Dahdah, E.; Aouad, S.; Gennequin, C.; Estephane, J.; Abi-Aad, E. Glycerol steam reforming over Ru–Mg–Al hydrotalcite–derived mixed oxides: Role of the preparation method in catalytic activity. *Int. J. Hydrogen Energy* **2018**, *43*, 19864–19872. [\[CrossRef\]](#)
39. Demsash, H.D.; Kondamudi, K.V.K.; Upadhyayula, S.; Mohan, R. Ruthenium doped nickel–alumina–ceria catalyst in glycerol steam reforming. *Fuel Proc. Technol.* **2018**, *169*, 150–156. [\[CrossRef\]](#)
40. Gallegos-Suárez, E.; Guerrero-Ruiz, A.; Rodríguez-Ramos, I. Efficient hydrogen production from glycerol by steam reforming with carbon supported ruthenium catalysts. *Carbon* **2016**, *96*, 578–587. [\[CrossRef\]](#)
41. Martínez, T.L.M.; Araque, M.; Centeno, M.A.; Roger, A.C. Role of ruthenium on the catalytic properties of CeZr and CeZrCo mixed oxides for glycerol steam reforming reaction toward H₂ production. *Catal. Today* **2015**, *242*, 80–90.
42. Gallo, A.; Pirovano, C.; Ferrini, P.; Marelli, M.; Dal Santo, V. Influence of reaction parameters on the activity of ruthenium based catalysts for glycerol steam reforming. *Appl. Catal. B Environ.* **2012**, *121–122*, 40–49. [\[CrossRef\]](#)
43. Byrd, A.J.; Pant, K.K.; Gupta, R.B. Hydrogen production from glycerol by reforming in supercritical water over Ru/Al₂O₃ catalyst. *Fuel* **2008**, *87*, 2956–2960. [\[CrossRef\]](#)
44. Bossola, F.; Pereira-Hernández, X.I.; Evangelisti, C.; Wang, Y.; Dal Santo, V. Investigation of the promoting effect of Mn on a Pt/C catalyst for the steam and aqueous phase reforming of glycerol. *J. Catal.* **2017**, *349*, 75–83. [\[CrossRef\]](#)
45. Buffoni, I.N.; Gatti, M.N.; Santori, G.F.; Pompeo, F.; Nichio, N.N. Hydrogen from glycerol steam reforming with a platinum catalyst supported on a SiO₂–C composite. *Int. J. Hydrogen Energy* **2017**, *42*, 12967–12977. [\[CrossRef\]](#)
46. Sad, M.E.; Duarte, H.A.; Vignatti, C.; Padró, C.L.; Apesteguía, C.R. Steam reforming of glycerol: Hydrogen production optimization. *Int. J. Hydrogen Energy* **2015**, *40*, 6097–6106. [\[CrossRef\]](#)
47. De Rezende, S.M.; Franchini, C.A.; Dieuzeide, M.L.; de Farias, A.M.D.; Fraga, M.A. Glycerol steam reforming over layered double hydroxide–supported Pt catalysts. *Chem. Eng. J.* **2015**, *272*, 108–118. [\[CrossRef\]](#)
48. Iriondo, A.; Barrio, V.L.; Cambra, J.F.; Arias, P.L.; Fierro, J.L.G. Influence of La₂O₃ modified support and Ni and Pt active phases on glycerol steam reforming to produce hydrogen. *Catal. Commun.* **2009**, *830*, 1275–1278. [\[CrossRef\]](#)
49. Pompeo, F.; Santori, G.F.; Nichio, N.N. Hydrogen production by glycerol steam reforming with Pt/SiO₂ and Ni/SiO₂ catalysts. *Catal. Today* **2011**, *172*, 183–188. [\[CrossRef\]](#)
50. Wei, Z.; Karim, A.M.; Li, Y.; King, D.L.; Wang, Y. Elucidation of the roles of Re in steam reforming of glycerol over Pt–Re/C catalysts. *J. Catal.* **2015**, *322*, 49–59. [\[CrossRef\]](#)
51. Pastor-Pérez, L.; Sepúlveda-Escribano, A. Low temperature glycerol steam reforming on bimetallic PtSn/C catalysts: On the effect of the Sn content. *Fuel* **2017**, *194*, 222–228. [\[CrossRef\]](#)

52. Bac, S.; Say, Z.; Kocak, Y.; Ercan, K.E.; Avci, A.K. Exceptionally active and stable catalysts for CO₂ reforming of glycerol to syngas. *Appl. Catal. B Environ.* **2019**, *256*, 117808. [\[CrossRef\]](#)
53. Silva, J.M.; Ribeiro, L.S.; Órfão, J.J.M.; Soria, M.A.; Madeira, L.M. Low temperature glycerol steam reforming over a Rh-based catalyst combined with oxidative regeneration. *Int. J. Hydrogen Energy* **2019**, *44*, 2461–2473. [\[CrossRef\]](#)
54. Senseni, A.Z.; Meshkani, F.; Fattahi, S.M.S.; Rezaei, M. A theoretical and experimental study of glycerol steam reforming over Rh/MgAl₂O₄ catalysts. *Energy Convers. Manag.* **2017**, *154*, 127–137. [\[CrossRef\]](#)
55. Martínez, T.L.M.; Araque, M.; Vargas, J.C.; Roger, A.C. Effect of Ce/Zr ratio in CeZr-CoRh catalysts on the hydrogen production by glycerol steam reforming. *Appl. Catal. B Environ.* **2013**, *132–133*, 499–510. [\[CrossRef\]](#)
56. Zhang, B.; Tang, X.; Li, Y.; Xu, Y.; Shen, W. Hydrogen production from steam reforming of ethanol and glycerol over ceria-supported metal catalysts. *Int. J. Hydrogen Energy* **2007**, *32*, 2367–2373. [\[CrossRef\]](#)
57. Ebshish, A.; Yaakob, Z.; Taufiq-Yap, Y.H.; Bshish, A.; Shaibani, A. Catalytic steam reforming of glycerol over cerium and palladium-based catalysts for hydrogen production. *J. Fuel Cell Sci. Technol.* **2013**, *10*, 021003. [\[CrossRef\]](#)
58. Adhikari, S.; Fernando, S.; Haryanto, A. Production of hydrogen by steam reforming of glycerin over alumina-supported metal catalysts. *Catal. Today* **2007**, *129*, 355–364. [\[CrossRef\]](#)
59. Senseni, A.Z.; Rezaei, M.; Meshkani, F. Glycerol steam reforming over noble metal nanocatalysts. *Chem. Eng. Res. Des.* **2017**, *123*, 360–366. [\[CrossRef\]](#)
60. Charisiou, N.D.; Tzounis, L.; Sebastian, V.; Baker, M.A.; Hinder, S.J.; Polychronopoulou, K.; Goula, M.A. Investigating the correlation between deactivation and the carbon deposited on the surface of Ni/Al₂O₃ and Ni/La₂O₃-Al₂O₃ catalysts during the biogas reforming reaction. *Appl. Surf. Sci.* **2019**, *474*, 42–56. [\[CrossRef\]](#)
61. Charisiou, N.D.; Siakavelas, G.; Papageridis, K.N.; Baklavaridis, A.; Tzounis, L.; Avraam, D.G.; Goula, M.A. Syngas production via the biogas dry reforming reaction over nickel supported on modified with CeO₂ and/or La₂O₃ alumina catalysts. *J. Nat. Gas Sci. Eng.* **2016**, *31*, 164–183. [\[CrossRef\]](#)
62. Profeti, L.P.R.; Ticianelli, A.A.; Assaf, E.M. Production of hydrogen via steam reforming of biofuels on Ni/CeO₂-Al₂O₃ catalysts promoted by noble metals. *Int. J. Hydrogen Energy* **2009**, *34*, 5049–5060. [\[CrossRef\]](#)
63. Charisiou, N.D.; Baklavaridis, A.; Papadakis, V.G.; Goula, M.A. Synthesis gas production via the biogas reforming reaction over Ni/MgO-Al₂O₃ and Ni/CaO-Al₂O₃ catalysts. *Waste Biomass Valoriz.* **2016**, *7*, 725–736. [\[CrossRef\]](#)
64. Larimi, A.; Khorasheh, F. Renewable hydrogen production over Pt/Al₂O₃ nano-catalysts: Effect of M-promoting (M=Pd, Rh, Re, Ru, Ir, Cr). *Int. J. Hydrogen Energy* **2019**, *44*, 8243–8251. [\[CrossRef\]](#)
65. Polychronopoulou, K.; Zedan, A.F.; Katsiotis, M.S.; Baker, M.A.; AlKhoori, A.A.; Siham, Y.; Qaradawi, A.; Hinder, S.J.; AlHassan Saeed, J. Rapid microwave assisted sol-gel synthesis of CeO₂ and Ce_xSm_{1-x}O₂ nanoparticle catalysts for CO oxidation. *Mol. Catal. A Chem.* **2017**, *428*, 41–55. [\[CrossRef\]](#)
66. Goula, G.; Botzolaki, G.; Osatiashtiani, A.; Parlett, C.M.A.; Kyriakou, G.; Lambert, R.M.; Yentekakis, I.V. Oxidative thermal sintering and redispersion of Rh nanoparticles on supports with high oxygen ion lability. *Catalysts* **2019**, *9*, 541. [\[CrossRef\]](#)
67. Yentekakis, I.V.; Goula, G.; Hatzisymeon, M.; Betsi-Argyropoulou, I.; Botzolaki, G.; Kousi, K.; Kondarides, D.I.; Taylor, M.J.; Parlett, C.M.A.; Osatiashtiani, A.; et al. Effect of support oxygen storage capacity on the catalytic performance of Rh nanoparticles for CO₂ reforming of methane. *Appl. Catal. B Environ.* **2019**, *243*, 490–501. [\[CrossRef\]](#)
68. Yentekakis, I.V.; Goula, G.; Panagiotopoulou, P.; Kampouri, S.; Taylor, M.J.; Kyriakou, G.; Lambert, R.M. Stabilization of catalyst particles against sintering on oxide supports with high oxygen ion lability exemplified by Ir-catalysed decomposition of N₂O. *Appl. Catal. B Environ.* **2016**, *192*, 357–364. [\[CrossRef\]](#)
69. Charisiou, N.D.; Siakavelas, G.; Tzounis, L.; Sebastian, V.; Monzon, A.; Baker, M.A.; Hinder, S.J.; Polychronopoulou, K.; Yentekakis, I.V.; Goula, M.A. An in depth investigation of deactivation through carbon formation during the biogas dry reforming reaction for Ni supported on modified with CeO₂ and La₂O₃ zirconia catalysts. *Int. J. Hydrogen Energy* **2018**, *43*, 18955–18976. [\[CrossRef\]](#)
70. Charisiou, N.D.; Iordanidis, A.; Polychronopoulou, K.; Yentekakis, I.V.; Goula, M.A. Studying the stability of Ni supported on modified with CeO₂ alumina catalysts for the biogas dry reforming reaction. *Mater. Today Proc.* **2018**, *5*, 27607–27616. [\[CrossRef\]](#)
71. Demsash, H.D.; Mohan, R. Steam reforming of glycerol to hydrogen over ceriapromoted nicklealumina catalysts. *Int. J. Hydrogen Energy* **2016**, *41*, 22732–22742. [\[CrossRef\]](#)

72. Iriondo, A.; Barrio, V.L.; Cambra, J.F.; Arias, P.L.; Guemez, M.B.; Sanchez-Sanchez, M.C.; Navarro, R.M.; Fierro, J.L.G. Glycerol steam reforming over Ni catalysts supported on ceria and ceria-promoted alumina. *Int. J. Hydrogen Energy* **2010**, *35*, 11622–11633. [\[CrossRef\]](#)
73. Kamonsuangkasem, K.; Therdthianwong, S.; Therdthianwong, A.; Thammajak, N. Remarkable activity and stability of Ni catalyst supported on CeO₂–Al₂O₃ via CeAlO₃ perovskite towards glycerol steam reforming for hydrogen production. *Appl. Catal. B Environ.* **2017**, *218*, 650–663. [\[CrossRef\]](#)
74. Chen, W.; Zhao, G.; Xue, Q.; Chen, L.; Lu, Y. High carbon-resistance Ni/CeAlO₃–Al₂O₃ catalyst for CH₄/CO₂ reforming. *Appl. Catal. B Environ.* **2013**, *136–137*, 260–268. [\[CrossRef\]](#)
75. Iliopoulou, E.F.; Efthimiadis, E.A.; Nalbandian, L.; Vasalos, I.A.; Barth, J.O.; Lercher, J.A. Ir-based additives for NO reduction and CO oxidation in the FCC regenerator: Evaluation, characterization and mechanistic studies. *Appl. Catal. B Environ.* **2005**, *60*, 277–288. [\[CrossRef\]](#)
76. Goula, M.A.; Charisiou, N.D.; Papageridis, K.N.; Delimitis, A.; Papista, E.; Pachatouridou, E.; Iliopoulou, E.; Marnellos, G.E.; Konsolakis, M.; Yentekakis, I.V. A comparative study of the H₂-assisted SCR of NO by C₃H₆ over noble metal (Pt, Pd, Ir)/γ-Al₂O₃ catalysts. *J. Environ. Chem. Eng.* **2016**, *4*, 1629–1641. [\[CrossRef\]](#)
77. Han, X.; Wang, Y.; Zhang, Y.; Yu, Y.; He, H. Hydrogen production from oxidative steam reforming of ethanol over Ir catalysts supported on Ce–La solid solution. *Int. J. Hydrogen Energy* **2017**, *42*, 11177–11186. [\[CrossRef\]](#)
78. Polychronopoulou, K.; Zedan, A.F.; AlKetbi, M.; Stephen, S.; Ather, M.; Katsiotis, M.S.; Arvanitidis, J.; Christofilos, D.; Isakovitch, A.F.; AlHassan, S. Tailoring the efficiency of an active catalyst for CO abatement through oxidation reaction: The case study of samarium-doped ceria. *J. Environ. Chem. Eng.* **2018**, *6*, 266–280. [\[CrossRef\]](#)
79. Duarte, R.B.; Damyanova, S.; de Oliveira, D.C.; Marques, C.M.P.; Bueno, J.M.C. Study of Sm₂O₃-doped CeO₂–Al₂O₃-supported Pt catalysts for partial CH₄ oxidation. *Appl. Catal. A Gen.* **2011**, *399*, 134–145. [\[CrossRef\]](#)
80. Damyanova, S.; Bueno, J.M. Effect of CeO₂ loading on the surface and catalytic behaviors of CeO₂–Al₂O₃-supported Pt catalysts. *Appl. Catal. A Gen.* **2003**, *253*, 135–150. [\[CrossRef\]](#)
81. Ma, H.; Zeng, L.; Tian, H.; Li, D.; Wang, X.; Li, X.; Gong, J. Efficient hydrogen production from ethanol steam reforming over La-modified ordered mesoporous Ni-based catalysts. *Appl. Catal. B Environ.* **2016**, *181*, 321–331. [\[CrossRef\]](#)
82. Cai, W.; Hu, Y.; Wang, W.; Zhou, J.; Jaroniek, M. Template-free synthesis of hierarchical γ-Al₂O₃ nanostructures and their adsorption affinity toward phenol and CO₂. *RSC Adv.* **2015**, *5*, 7066–7073. [\[CrossRef\]](#)
83. Chen, F.; Wu, C.; Dong, L.; Vassallo, A.; Williams, P.T.; Huang, J. Characteristics and catalytic properties of Ni/CaAlOx catalyst for hydrogen-enriched syngas production from pyrolysis-steam reforming of biomass sawdust. *Appl. Catal. B Environ.* **2016**, *183*, 168–175. [\[CrossRef\]](#)
84. Jiao, Y.; Zhang, J.; Du, Y.; Li, F.; Li, C.; Lu, J.; Wang, J.; Chen, Y. Hydrogen production by catalytic steam reforming of hydrocarbon fuels over Ni/Ce–Al₂O₃ bifunctional catalysts: effects of SrO addition. *Int. J. Hydrogen Energy* **2016**, *41*, 13436–13447. [\[CrossRef\]](#)
85. Guo, R.T.; Zhou, Y.; Pan, W.G.; Hong, J.N.; Zhen, W.L.; Jin, Q.; Ding, C.G.; Guo, S.Y. Effect of preparation methods on the performance of CeO₂/Al₂O₃ catalysts for selective catalytic reduction of NO with NH₃. *J. Ind. Eng. Chem.* **2013**, *19*, 2022–2025. [\[CrossRef\]](#)
86. Jeon, S.; Roh, S.-H.; Moon, D.J.; Bae, J.W. Aqueous phase reforming and hydrodeoxygenation of ethylene glycol on Pt/SiO₂–Al₂O₃: effects of surface acidity on product distribution. *RSC Adv.* **2016**, *6*, 68433–68444. [\[CrossRef\]](#)
87. Frost, R.L.; Klopogge, J.; Russell, S.C.; Sztetu, J.L. Dehydroxylation and structure of alumina gels prepared from trisecbutoxyaluminium. *Thermochim. Acta* **1999**, *329*, 47–56. [\[CrossRef\]](#)
88. Liu, X. DRIFTS Study of Surface of γ-Alumina and Its Dehydroxylation. *J. Phys. Chem. C* **2008**, *112*, 5066–5073. [\[CrossRef\]](#)
89. Chen, J.; Hu, W.; Huang, F.; Li, G.; Yuan, S.; Gong, M.; Zhong, L.; Chen, Y. Catalytic performance of a Pt–Rh/CeO₂–ZrO₂–La₂O₃–Nd₂O₃ three-way compress nature gas catalyst prepared by a modified double-solvent method. *J. Rare Earths* **2017**, *35*, 857. [\[CrossRef\]](#)
90. Tao, H.; Sun, X.; Back, S.; Han, Z.; Zhu, Q.; Robertson, A.W.; Ma, T.; Fan, Q.; Han, B.; Jung, Y.; et al. Doping palladium with tellurium for the highly selective electrocatalytic reduction of aqueous CO₂ to CO. *Chem. Sci.* **2018**, *9*, 483–487. [\[CrossRef\]](#)

91. Shan, C.C.; Tsai, D.S.; Huang, Y.S.; Jian, S.H.; Cheng, C.L. Pt-Ir-IrO₂NT Thin-Wall Electrocatalysts Derived from IrO₂ Nanotubes and Their Catalytic Activities in Methanol Oxidation. *Chem. Mater.* **2007**, *19*, 424–431. [\[CrossRef\]](#)
92. Senseni, A.Z.; Meshkani, F.; Rezaei, M. Steam reforming of glycerol on mesoporous nanocrystalline Ni/Al₂O₃ catalysts for H₂ production. *Int. J. Hydrogen Energy* **2016**, *41*, 20137–20146. [\[CrossRef\]](#)
93. Bulutoglu, P.S.; Say, Z.; Bac, S.; Ozensoy, E.; Avci, A.K. Dry reforming of glycerol over Rh-based ceria and zirconia catalysts: New insights on catalyst activity and stability. *Appl. Catal. A Gen.* **2018**, *564*, 157–171. [\[CrossRef\]](#)
94. Dai, R.; Zheng, Z.; Yan, W.; Lian, C.; Wu, X.; An, X.; Xie, X. Dragon fruit-like Pt-Cu@mSiO₂ nanocomposite as an efficient catalyst for low-temperature ethanol steam reforming. *Chem. Eng. J.* **2020**, *379*, 122299. [\[CrossRef\]](#)
95. Bilal, M.; Jackson, S.D. Ethanol steam reforming over Pt/Al₂O₃ and Rh/Al₂O₃ catalysts: The effect of impurities on selectivity and catalyst deactivation. *Appl. Catal. A Gen.* **2017**, *529*, 98–107. [\[CrossRef\]](#)
96. Katryniok, B.; Paul, S.; Bellière-Baca, V.; Rey, P.; Dumeignil, F. Glycerol dehydration to acrolein in the context of new uses of glycerol. *Green Chem.* **2010**, *12*, 2079–2098. [\[CrossRef\]](#)
97. Dou, B.; Wang, C.; Song, Y.C.; Chen, H.S.; Xu, Y.J. Activity of Ni–Cu–Al based catalyst for renewable hydrogen production from steam reforming of glycerol. *Energy Convers. Manag.* **2014**, *78*, 253–259. [\[CrossRef\]](#)
98. Stosic, D.; Bennici, S.; Sirotin, S.; Calais, C.; Couturier, J.-L.; Doubois, J.-L.; Travert, A.; Auroux, A. Glycerol dehydration over calcium phosphate catalysts: Effect of acidic–basic features on catalytic performance. *Appl. Catal. A Gen.* **2012**, *447–448*, 124–134. [\[CrossRef\]](#)
99. Wang, F.; Cai, W.; Provendier, H.; Schuurman, Y.; Descorme, C.; Mirodatos, C.; Shen, W. Ageing analysis of a model Ir/CeO₂ catalyst in ethanol steam reforming. *Appl. Catal. B Environ.* **2012**, *125*, 546–555. [\[CrossRef\]](#)
100. Zou, J.; Zhang, S.; Zhang, J.; Chen, Y.; Cui, L.; Xu, T.; Cai, W. Hydrogen production from ethanol over Ir/CeO₂ catalyst: Effect of the calcination temperature. *Fuel* **2015**, *159*, 741–750. [\[CrossRef\]](#)



© 2020 by the authors. Licensee MDPI, Basel, Switzerland. This article is an open access article distributed under the terms and conditions of the Creative Commons Attribution (CC BY) license (<http://creativecommons.org/licenses/by/4.0/>).